5 Changes in Ultraviolet and Visible Solar Irradiance 1979 to 2008

Jay Herman

Goddard Space Flight Center
Code 613.3
Greenbelt, MD 20771 USA
E-mail: jay.r.herman@nasa.gov

Abstract A description is presented of instruments and requirements for measuring ultraviolet (UV) and visible irradiance and estimating long-term changes in irradiance from the ground-based and satellite data The 30-year changes in zonal average UV irradiances are estimated from changes that have occurred in ozone amount and cloud cover as a function of latitude and season. Ozone changes have been obtained from a multiple satellite time series starting with Nimbus-7/Total Ozone Mapping Spectrometer (TOMS) in 1979 and continuing to the end of 2008 with the Solar Backscatter Ultraviolet (SBUV-2) series, Earth-Probe TOMS, and Ozone Monitoring Instrument (OMI). The changes in cloud cover have been obtained using the 340 nm reflectivity data from the same series of satellite instruments, except for Earth-Probe TOMS. The results show large increases in UV-B (280 nm − 315 nm) irradiance in both hemispheres, mostly caused by changes in ozone amounts. The largest increases have occurred in the Southern Hemisphere for clear-sky conditions when compared to the same latitudes in the Northern Hemisphere. Since 1979, an increase of 5% − 8% has occurred in clear-sky DNA damage action spectra weighted irradiance P_{DNA} during most of the spring and summer, with increases ranging from 12% to 15% between 30°S and 40°S and 18% to 22% between 40°S and 50°S. Increases in erythemal irradiance are about half that of P_{DNA}. There were only small changes in the equatorial zone (±23°), where sea level UV irradiances are largest because of naturally low ozone amounts and the nearly overhead sun.

Keywords ultraviolet, trends, RAF, erythemal, spectrometer, pyranometer

5.1 Introduction

Determining the amount of ultraviolet (290 nm − 400 nm) and visible (VIS,

400 nm − 700 nm) radiation that reaches the earth's surface is a fundamental problem that has occupied scientists and governments from the earliest times. In highly organized major civilizations, the primary reason for the intense interest was to determine the factors (sunlight, drought, and temperature) that affected agriculture, and through agriculture, the wealth and population of nations. The quantitative interest in changing amounts of solar radiation is a more modern endeavor that still has an agricultural underpinning, but has expanded into direct human health effects, effects on land and ocean biology, materials damage, and global warming. In addition to these long-term effects (years-to-decades) from changing solar radiation, there are short-term phenomena (minutes-to-yearly), such as the effects of solar radiation on boundary layer and tropospheric photochemistry, clouds and aerosols, and local and global weather. Short-term changes in ozone and cloud cover change the amount of solar radiation reaching the earth's surface and affect each year's agriculture, the extent of human and other biological exposure, and damage to materials. The extent of human exposure and the corresponding health effects are difficult to quantify because of the mobility of people, the great variety of resistance to UV damage caused by skin type (Hemminki, 2002) and other genetic factors, in addition to the effects of culture and diet on mitigating UV exposure. An example is seen in the relative incidence of skin cancer between Japanese and Caucasians living in the U.S. For the Japanese, the non-melanoma skin cancer rate is about 1 per 100,000, while for Caucasians the rate is about 15 per 100,000 (Qiu and Marugame, 2008). Even the low cancer rate reported for the Japanese-American ethnic group is about double the rate reported in Japan.

Instrumental methods for measuring or estimating solar radiation amounts have gradually evolved from simple ground-based instrumentation that essentially measured the heating effect of all solar radiation (e.g., pyranometers and standardized water evaporation containers, Fig. 5.1) to spectrometers capable of good spectral resolution (0.5 nm) in the UV and VIS range. Before 1979, the only sources of UV and VIS data were obtained from sparsely scattered ground stations of varying accuracy and precision. The longest reconstructed time series of solar UV irradiance from measurements of ozone amounts goes back to 1928 at Arosa, Switzerland (Staehelin and Weiss, 2001; Staehelin et al., 1998), and another near Moscow, Russia goes back to 1968 (Chubarova, 2008) based on direct UV measurements. There have been calibrated measurements of total column ozone since the late 1950s at several stations from which clear-sky UVB (280 nm − 315 nm) can be derived. Attempts have been made to reconstruct the ozone time series back to the late 1600s by estimating the UV-B (280 nm − 315 nm) stress on biological systems, particularly on pine and spruce trees (Zuev and Bonderenko, 2001), and by other biological proxies (Rozema et al., 2002). Networks of standardized evaporation pans (Roderick and Farquhar, 2002), and pyranometers (Stanhill and Cohen, 2001) appear to have detected a long-term reduction in solar irradiance at the earth's surface that seems to be associated with increased cloud and aerosol amounts; a concept popularly known as "global dimming."

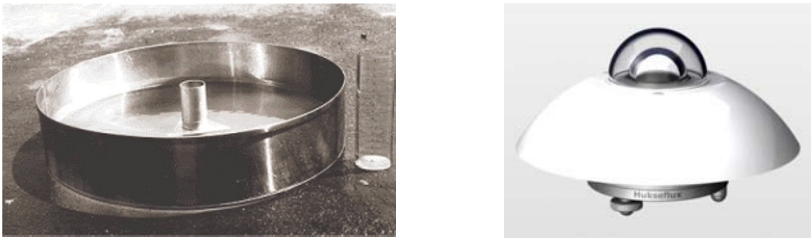

(a) (b)

Figure 5.1 (a) Standardized evaporation pan for measurement of water evaporation installed on a wooden platform in a grassy location. The pan is filled with water and exposed to sunlight; (b) An example of a pyranometer used for measuring total solar irradiance

Then and now, the preponderance of UV measuring stations are located in the Northern Hemisphere, mostly in Europe and North America, with gradually increasing numbers in Asia. There are a few stations in South America (Argentina, Chile, and Brazil), New Zealand, Australia, and Africa. A well-calibrated polar network of seven stations has been maintained by the U.S. National Science Foundation in Antarctica (Palmer, McMurdo, and South Pole Stations); Ushuaia, Argentina; Barrow, Alaska; Summit, Greenland; and San Diego, California. These have been augmented in recent years by the worldwide distribution of well-calibrated sun and sky photometers as part of AErosol RObotic NETwork (AERONET) (Holben et al., 1998). Reliable satellite measurements of ozone derived from back-scattered UV radiation started in late 1978, with an earlier attempt from the BUV instrument (1970 − 1977) on the Nimbus-4 satellite. Since November 1978, satellite UV data consists of daily measurements of ozone amount and cloud reflectivity from Nimbus-7/Total Ozone Mapping Spectrometer (TOMS) and the Solar Backscatter Ultra-Violet (SBUV) instrument, continued with the NOAA SBUV-2 series, Ozone Monitoring Instrument (OMI), and Global Ozone Monitoring Experiment (GOME). These data provide global coverage using an independent calibration for each instrument that can be validated with respect to existing ground stations. Global coverage has been especially important for understanding processes over the oceans, in Africa, parts of Asia, and most of the Southern Hemisphere, where ground-based data are sparse or non-existent. The availability of satellite data has intensified the efforts to develop reliable ground-based instrumentation and to perfect their calibration, for direct measurements of both UV irradiance and atmospheric composition (ozone, sulfur dioxide, aerosols, and more recently, nitrogen dioxide and formaldehyde).

Satellite measurements of ozone amount, reflectivity, and some aerosol properties have enabled good estimates of radiation reaching the ground using laboratory measured absorption and scattering coefficients in radiative transfer calculations that include polarization effects. The principal sources of error in satellite-based estimates of UV and VIS radiation are from the properties and amounts of absorbing aerosols, which are not easily measured from satellites. When satellite measurements of ozone and reflectivity are combined with ground-based

measurements of aerosols (or in very clean atmospheres), estimates of UV and VIS radiation reaching the ground compare well with ground-based data (Kalliskota et al., 2000). The best estimates of VIS wavelength aerosol properties in the atmosphere come from a large network of AERONET CIMEL sunphotometers that are strategically located in many parts of the world. The AERONET data consist of estimates of aerosol extinction at six wavelengths (340, 380, 440, 670, 870 and 1,020 nm), absorption optical depths at four wavelengths (440, 670, 870 and 1,020 nm) and particle size distribution. These aerosol parameters are essential for VIS and UV radiative transfer calculations. However, extrapolation of aerosol absorption from the VIS to the UV has proved to be incorrect (Krotkov et al., 2005; Cede et al., 2006) leading to errors in calculated UV fluxes at the surface and photolysis rates in the troposphere.

Currently, comparisons of satellite-based estimates of UV irradiance with ground-based measurements show overestimates that can range up to 40% when unmeasured aerosol loadings are large. For unpolluted sites, the agreement is within 2% or 3%, consistent with known instrument calibration errors for both satellite and ground-based instruments. For UV radiation, this is implies that the relation between ozone and absorption of UV-B is well understood, as is the relationship between UV-A (315 nm − 400 nm) and VIS irradiances and aerosols (scattering and absorbing). For a comparison of ground-based measurements with satellite estimates of solar radiation, the major outstanding problems are outlined as follows:

(1) Accounting for the aerosol absorption optical depth from 300 nm to 1,000 nm.
(2) Satellite estimation of UV and VIS radiation over snow and ice.
(3) Measurements of ozone, reflectivity, and UV+VIS radiation at high latitudes and solar zenith angles (SZAs) (latitudes of 65° and SZA >70°) both from the ground and from satellites.
(4) Establishment of international transfer standards and transfer methods that are better than the current limit of about 3%.
(5) Creating common stable calibrations between all types of ground-based instruments at different locations.
(6) Accounting for the differences between ground-based and satellite measurements caused by their different fields of view (FOV).
(7) Improved understanding of radiance and irradiance transmission by clouds, which becomes increasingly important as the FOV becomes smaller.

The amount of solar ultraviolet UV and VIS radiation reaching the earth's surface, and the fraction reflected back to space, is primarily governed by the amount of cloud cover, and to a lesser extent, by Rayleigh scattering, aerosols, and various absorbing gases (e.g., O_3, NO_2, H_2O). Unlike the weakly surface reflected UV and blue radiation, most of the VIS solar radiation is moderately reflected by the ground and vegetation. For UV-B irradiance, ozone, aerosols, and cloud cover are the most important atmospheric components limiting the amount radiation able to reach the ground. Ultraviolet-A irradiances reaching the

ground are limited by aerosols and cloud cover.

Figure 5.2 shows an example of solar flux measured above the atmosphere by the Solar-Stellar Irradiance Comparison Experiment (SOLSTICE) (McClintock et al., 2000) and the space shuttle borne Atlas-3/Solar Ultraviolet Spectral Irradiance Monitor (SUSIM) (Brueckner et al., 1994) spectrometers, and the calculated solar irradiance reaching the ground for overhead sun and 300 Dobson Units (DU) of ozone. Atlas-3/SUSIM was a high spectral resolution instrument (0.15 nm), which clearly shows the solar Fraunhofer line structure, especially the calcium K and H lines at 393.3 nm and at 396.9 nm (see inset in Fig. 5.2). SOLSTICE was an independent lower resolution instrument that agrees quite well with Atlas-3/SUSIM. These data are a good starting point for UV radiative transfer calculations in the atmosphere to provide estimates of UV irradiance reaching the ground.

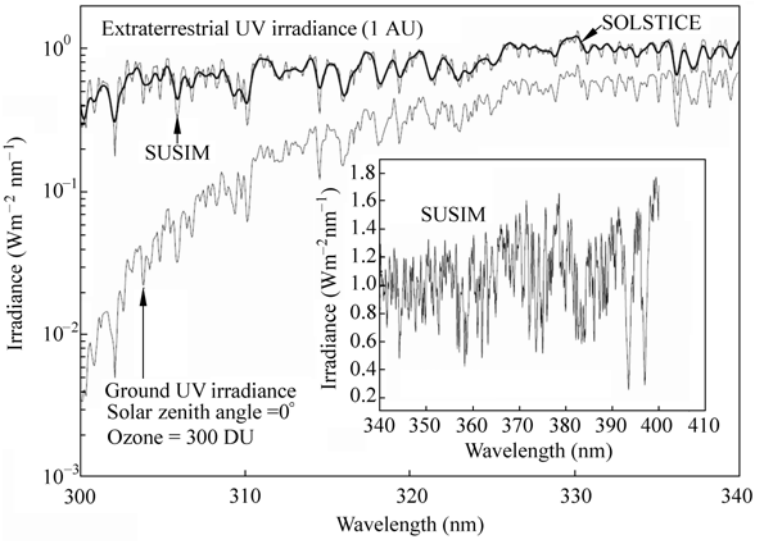

Figure 5.2 The extraterrestrial solar UV irradiance measured by SOLSTICE and Atlas-3/SUSIM instruments above the atmosphere normalized to a sun-earth distance of 1 astronomical unit, and the calculated irradiance at the ground for 300 DU of ozone and overhead sun. Only the inset, 340 nm − 410 nm is shown at full resolution of 0.15 nm. 1 DU = 2.67×10^{16} molecules/cm^2

Ozone absorbs a wavelength-dependent fraction of the solar UV radiation in the 200 nm to 340 nm range, with peak absorption at 255.4 nm. Almost no solar photons with wavelengths shorter than 280 nm reach the earth's surface because of ozone (Hartley and Huggins bands) and molecular oxygen absorption (Schumann-Runge band and continuum absorption). There is still strong absorption at 310 nm, where a 1% change in ozone leads to an approximate 1% change in irradiance for SZA = 45°. At wavelengths less than 305 nm, the increasingly large ozone absorption coefficient leads to a proportionally large increase in irradiance for a

small decrease in ozone (e.g., at SZA = 45°, a 1% decrease in ozone can produce a 2.2% increase in 305 nm irradiance).

Clouds and scattering aerosols reduce solar radiation at all wavelengths λ by reflecting a fraction of the energy back to space, which depends on the aerosol's refractive index and particle size. Except in cases of dense smoke or dust, scattering aerosols (e.g., sulfates) usually reduce radiation reaching the surface by less than 10%. Under special conditions, clouds can locally increase UV from 1% to 10% by cloud edge reflections. Extremely heavy cloud cover (black thunderstorm) can decrease UV and VIS by almost 100%, while even moderate cloud thickness can change the UV-B spectral distribution because of the additional ozone absorption caused by multiple scattering.

In addition to the above effects, VIS wavelengths are modulated by H_2O, and those in the Near-IR (NIR) (700 nm − 3,000 nm) are modulated by changes in CO_2, CH_4, and H_2O, within their respective absorption bands. There is an additional small amount of absorption for UV-A and blue wavelengths from NO_2 and HCHO, and for UV-B from SO_2, in addition to a stronger absorption for UV and VIS from smog in urban or industrial areas.

Ultraviolet and VIS radiation at the surface are generally highest near the equator following the seasonally changing sub-solar point (latitude between ±23.3°), where ozone amounts are low and the SZA is the smallest. For any specific latitude, larger amounts of solar radiation are seen at high altitude sites because of reduced Rayleigh scattering, especially those with predominantly dry and clear weather and large surface reflectivity (e.g., from snow or ice cover).

Understanding, modeling, and measuring the factors that affect the amount of UV and VIS radiation reaching the earth's surface are important, since changes in these radiation amounts impact agricultural and ocean productivity, global energy balance, and human health. Changes in UV radiation can affect human health adversely through skin cancer (Diffey, 1991), eye cataracts (Taylor, 1990), and suppression of the immune system (Vermeer et al., 1991), yet positively through increased vitamin D production (Grant, 2002; Holick, 2004). Changes in UV radiation can also significantly affect ecosystem biology (Smith et al., 1992; Ghetti et al., 2006).

The focus of this chapter is the estimation or detection of UV irradiance changes that can be measured directly from the ground, or estimated using satellite-based or ground-based measurements that characterize the optical properties of the atmosphere. Section 5.2 describes a subset of the instrumentation widely deployed today, as well as two new instruments recently deployed and validated for measurements of atmospheric optical properties. Section 5.3 is devoted to a discussion of estimating long-term trends in UV irradiance based on satellite derived ozone and reflectivity amounts. The concept of radiation amplification factor (RAF) is reviewed for the purpose of estimating monochromatic irradiance changes from Beer's Law. A second, apparently empirical, power law form is introduced for deriving irradiance trends when changes are estimated for action

spectra weighted wavelength integrated irradiances. In a later section, it is shown that the empirical power law form can be numerically derived from the Beer's Law form. Section 5.4 presents a brief discussion of UV irradiance in the Polar Regions. Section 5.5 briefly discusses the effects of UV irradiance on human health. Section 5.6 discusses the UV Index and commonly used units for irradiance and exposure (time integral of irradiance). Section 5.7 introduces the concept of action spectra and discusses their application, gives accurate fitting functions for four of these spectra, derives the power law RAF for each of these spectra, and shows a comparison of theory with data obtained for the erythemal action spectrum. Estimated annual zonal average irradiance changes are presented for monochromatic irradiances (305 nm − 325 nm), erythemal irradiances, and monthly zonal average irradiance (305 nm), as well as the DNA damage action spectrum.

5.2 Instrumentation

Instrumentation for measuring solar radiation reaching the ground falls into a few main classes, which have been described at length in specialized literature and reports. The earliest reliable device for quantitative measurements of solar radiation was a pyranometer (Kerr et al., 1967), which converted the sun's photon energy into heat and then into a voltage or current proportional to the energy-weighted integrated solar photon flux (Fig. 5.1(a)). Pyranometers are still deployed at many sites, some of which have the longest broadband data records for well-calibrated highly stable instruments. The basic pyranometer measurement is the solar irradiance in watts/m^2 over a hemispherical field of view, which includes both direct and diffuse (scattered) photons, and a wavelength range from 280 nm to 3,000 nm. The detector is a black-coated thermopile with a nearly perfect cosine response for photons incident at different angles. The pyranometer's stability makes it ideal for detecting small long-term changes in solar irradiance caused by changes in the atmosphere (clouds and aerosols), changes in surface reflectivity, and of course, changes in solar output. The stability suggests an application for determining the amount of UV irradiance by combining pyranometer data for cloud transmission estimates with an instrument capable of determining the column amount of ozone Ω, and radiative transfer calculations. Ω is usually determined from the ratio of two or more measured narrow-band narrow FOV direct-sun viewing solar irradiances, and more recently by matching the entire absorption spectrum for a moderate wavelength range. This reduces two calibration problems: (1) the need for absolute radiometric calibration, and (2) the need for determining UV measuring instrument's cosine response to direct and diffuse radiances from different angles. While the combination is not a direct measurement of UV irradiance, it offers a solution to difficult calibration and stability problems inherent in direct measurements.

All other instruments that attempt to directly measure the direct plus diffuse photons (known as global flux) have a common calibration problem; namely, determining cosine response to the angle of the incident photons on a diffuser material (flat plate or some specially shaped diffuser). Most instruments rely on a laboratory-derived correction to their approximation of the ideal cosine response (e.g., Brewer spectrometers) instead of achieving a nearly perfect cosine response from hardware. An example of the latter is given by a commercially available UV spectrometer (290 nm − 400 nm with 1 nm resolution) developed at the National Institute of Water and Atmospheric Research in New Zealand. Unprotected diffuser materials (e.g., Teflon) are usually porous and susceptable to transmission changes from atmospheric pollution and from natural aging, which affects both the radiometric calibration and the cosine response. Such instruments require periodic recalibration to correct for changes in diffuser properties, detector sensitivity, and changes in the internal optics. One popular commercial instrument, the Multi-Filter Rotating Shadowband Radiometer (UV-MFRSR), uses an exposed diffuser element (no quartz window or dome in front of the Teflon diffuser) with the result that the optical transmission decreases from pollution effects and partly recovers after every rainfall. Hand-cleaning the diffuser with alcohol is only partialy effective.

Currently deployed instruments include broadband instruments, which measure the solar radiation from all directions using a diffuser over a specific wavelength range, which is usually less than viewed by a pyranometer. Most are tailored to have a response to different wavelengths that approximates some biological or application absorption spectrum (action spectrum $A(\lambda)$). The most frequently approximated action spectrum is the erythemal action spectrum, which provides a measurement of the skin reddening effect for exposure to UV-A and UV-B (McKinlay and Diffey, 1987). Next are multi-spectral filter instruments that measure solar radiation from all directions, or in a narrow field of view, using several narrow wavelength bands (usually less than 10 bands from 1 nm to 10 nm wide) at the same time or sequentially (e.g., the Yankee Environmental System Ultraviolet-Multifilter Rotating Shadowband Radiometer (UV-MFRSR), and the CIMEL Sunphotometer, Fig. 5.3). These instruments require calibration for the detector response, filter transmission function, and diffuser element (if any). All of these instruments, except for the pyranometer, suffer from out of band wavelength responses, scattered and stray light in the optics and detectors, and noise in either analog amplifiers or analog to digital converters. These problems can affect data quality and instrument stability if the instruments are not frequently monitored and calibrated.

The CIMEL sunphotometer, Fig. 5.3(a), is used by AERONET for worldwide aerosol characterization (440, 500, 675, 870, and 1,020 nm) for measuring atmospheric aerosol optical thickness, absorption, particle size, and a filter at 939 nm for measuring atmospheric water vapor. There are two additional channels (340 nm and 380 nm) that are only used for aerosol extinction optical depth. The

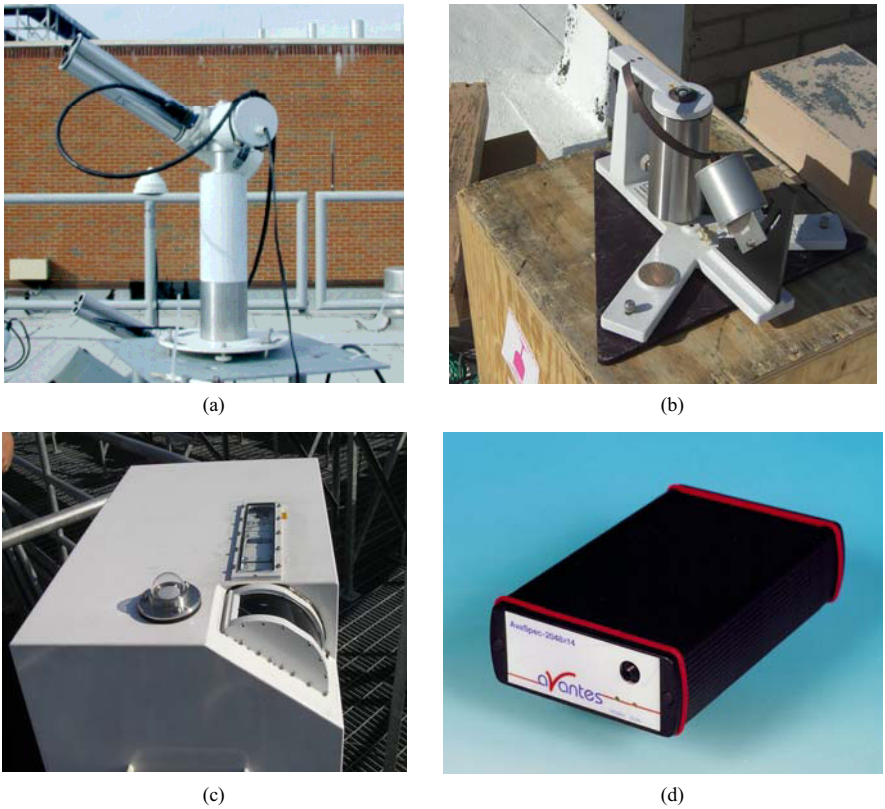

Figure 5.3 (a) Commercial AERONET CIMEL Sunphotometer for direct-sun and sky irradiances using two independent apertures, mounted on a sun-tracker; (b) Commercial modified UV-MFRSR (Shadowband) mounted on a fixed baseplate located at GSFC. The 300 nm channel has been replaced by 440 nm and a quartz dome is over the diffuser; (c) Commercial Brewer double monochromator measuring from 270 nm – 365 nm with a 0.5 nm resolution. This Brewer has been modified at GSFC with a curved quartz window and depolarizer to permit accurate measurements of sky radiances; (d) Miniature commercial spectrometer measuring from 270 nm – 525 nm with 0.5 nm resolution. The spectrometer is connected to an optical head by a fiber optic cable. This, or other commercial spectrometers, form the basis of the Pandora spectrometer system

instrument automatically determines and tracks the sun's position, and collects data in automated sequences of measurements, which include almucantar and principal plane with a 1.2° FOV. The CIMEL sunphotometers are calibrated at a central facility at Goddard Space Flight Center (GSFC) in the laboratory and against standard CIMELS, which are calibrated at Mauna Loa, Hawaii using the Langley method (Slusser et al., 2000). While the AERONET CIMELs have been extremely successful in determining aerosol properties (optical depth, absorption, and particle size distribution) in the VIS wavelengths, they cannot determine

aerosol absorption at UV wavelengths.

The UV-MFRSR (Fig. 5.3(b)) measures global radiation in seven wavelength bands (300, 305, 311, 317, 325, 332, 368 nm with 2 nm bandpass) using a cosine approximating diffuser assembly over seven separate detectors. The instrument measures whole sky (2π steradians) with and without the sun blocked by a curved metal band, which permits estimating the direct sun irradiance from the difference. The U.S. Department of Agriculture UV-B Monitoring and Research Program (UVMRP) has developed and maintains the largest network of UV-MFRSR's (over 36), which are field calibrated using the Langley method (Slusser et al., 2000) to measure global and direct sun irradiance and derive aerosol optical depths and ozone amounts from the short wavelength channels (Goering et al., 2005). While the primary purpose was for the furtherance of agricultural productivity in the US, the network has also provided a long-term database useful for irradiance related human health studies and satellite validation of ozone and UV irradiance estimates along with other traditional Brewer and Dobson spectrometers (Gao et al., 2001).

The combination of global and direct-sun irradiance can be used to deduce UV aerosol attenuation and absorption optical depths when the UV-MFRSR calibration is matched to the CIMEL sunphotometer. At GSFC and Colorado State University, the UV-MFRSR has been modified to improve its performance for aerosol detection by replacing the 300 nm channel with one for 440 nm to match one of the CIMEL sunphotometer's almucantar wavelength channels. With this modification, the UV-MFRSR can extend the CIMEL aerosol characterization into the UV wavelengths while matching the CIMEL results at 440 nm. The combined use of the CIMEL and the modified UV-MFRSR resulted in finding that the absorption of many urban aerosols have spectral dependencies in the UV that are different than those extrapolated from the visible CIMEL channels (Krotkov et al., 2005; Cede et al., 2006). The differences can be used to identify whether the aerosols are black carbon or the more strongly absorbing organic hydrocarbons. The results can also be used to calculate the reduction of UV irradiance by absorbing aerosols and to improve the estimation of tropospheric photolysis rates.

While useful work is still being done with filter spectroradiometers and broadband instruments, much more information can be derived from high spectral resolution spectrometers (e.g., the global network of Brewer spectrometers represented in the U.S. by the NOAA-EPA network of single-grating Brewers, the NSF/Biospherical network, at NASA by a modified (polarization insensitive) double-grating Brewer (Fig. 5.3(c)) (Cede et al., 2006), and by recently developed instruments using high quality commercial Charge Coupled Device (CCD) and Complementary Metal Oxide Semiconductor (CMOS) spectrometers (Fig. 5.3(d)).

The most versatile UV-VIS instruments are full spectrometers (prism, single- and double-grating dispersion elements) that are able to measure continuously in wavelength over a specified range in both narrow (less than 2°) and whole-sky FOV. The best known of these are the widely deployed Brewer spectrometers (single- and double-scanning grating versions with a single detector), which are

capable of both narrow FOV and whole-sky viewing through separate ports (Fig. 5.3(c)). The Brewer double grating instrument (283 nm – 364 nm) with resolution of about 0.5 nm full width half maximum (FWHM) is especially capable for measurements of ozone in the 300 nm – 315 nm range because of its extremely low amount of scattered or stray light (photons of one wavelength affecting the count rates of another wavelength). These instruments measure one wavelength at a time and can suffer random errors from the effects of a changing atmosphere during the duration of a measurement. This effect is minimized, but not eliminated, by a slit mask used to measure six closely spaced wavelengths in a short period of time. At GSFC, each Brewer wavelength is integrated multiple times for 0.1147 seconds, or about 0.7 seconds for all six wavelengths anywhere in the Brewer spectrometer's range. A modified version of the Brewer spectrometer has been built at GSFC, which removes the polarization sensitivity of the narrow FOV port by adding a depolarizer in front of the grating and a curved fused silica window, to replace the standard flat-plate window so that the viewing direction is always perpendicular to the window surface (Fig. 5.3(c)). This eliminates the Fresnel effect for diffuse polarized skylight. The modification permits the measurement of accurate sky radiances in the presence of an unknown amount or type of aerosol. The GSFC Brewer has successfully used measured sky-radiances to determine ozone profiles in the troposphere and stratosphere every 20 minutes throughout the day (Tzortziou et al., 2008). Another commercially available moderate size double monochromator spectrometer system has been developed in New Zealand by the National Institute of Water and Atmospheric Research (NIWA) that is technically competitive with the Brewer spectrometer. It has a wider spectral range (280 nm – 450 nm), but a coarser spectral resolution (1 nm FWHM).

There is a new class of portable narrow or wide FOV instruments that simultaneously measure all wavelengths in a specified range using a single grating as the dispersion device and a multi-pixel CCD or CMOS detector. When carefully characterized and calibrated, the narrow FOV CCD/CMOS spectrometer-based systems can measure UV and VIS radiances and derive trace gas amounts (O_3, SO_2, HCHO, BrO, NO_2, H_2O), aerosol properties (optical depth, absorption, and particle size) (Herman et al., 2009a), and ozone altitude profiles.

A small portable spectrometer based system (Pandora, Figs. 5.3(d) and 5.4(a)) that is accurate, but inexpensive, has been developed at GSFC. The CCD version consists of a temperature controlled 1/8 m symmetric Czerny-Turner commercial spectrometer (Fig. 5.3(d)) using a backthinned 2048×14 pixel CCD detector (270 nm to 525 nm with a resolution of 0.5 nm FWHM) coupled to a small custom-built optical head (Fig. 5.4(a), 1.6° circular FOV collimator, lens and filter wheel system, and electronics) by a 10 m UV-VIS transmitting fiber optic cable. The head is mounted on a computer controlled small sun-tracker device, which also permits pointing to anywhere in the sky (the fiber optic cable depolarizes the input). The plans, machine drawings, specifications, and software are freely available upon request.

For an accurate detection of trace gas amounts, the slit function, wavelength, and radiometric calibration must be accurately determined and maintained during operation by an active temperature control (20°C± 1°C) of the entire spectrometer. High signal to noise (SNR) and precision are achieved by averaging successive measurements (a few milliseconds exposure) over several seconds. The small automated sun tracker permits the instrument to operate in direct-sun viewing, almucantar, and principal plane modes for determination of aerosol properties in the same manner as the CIMEL, but as a continuous function of wavelength in both the VIS and UV ranges. The narrow FOV precludes measuring irradiance directly; but indirectly, the irradiance can be deduced by combining solar irradiance and sky radiance measurements with radiative transfer calculations.

A much larger portable spectrometer system (MFDOAS, Fig. 5.4(b); Herman et al., 2009a) with even higher precision for a given exposure time, but with the same accuracy, has been developed at Washington State University. It measures both sun and sky radiances (see Tables 5.1 and 5.2). The MFDOAS instrument consists of separate telescopes for direct sun or scattered sky, a filter wheel containing various filters and polarizers, a spectrometer/CCD-detector system, a pointing device, a computer, and a water-based cooler to maintain constant temperature.

MF-DOAS incorporates a modified commercial, single-pass Czerny-Turner spectrograph with a focal length of 300 mm (f/4). A 400-groove/mm diffraction grating, with a blaze wavelength of 400 nm, is used to disperse light. The spectrometer has a fixed 100 μm entrance slit, resulting in a 0.83 nm (7.8 pixels

(a)

(b)

Figure 5.4 (a) Pandora optical head and sun-tracker mounted on a tripod and attached to a small spectrometer (Fig. 5.3(d)) with a 10 m fiber optic cable; (b) MFDOAS spectrometer mounted on its base and sun-tracker. The water-cooled spectrometer is controlled by with a computer in its base

Table 5.1 Pandora characteristics

Wavelength interval	270 nm – 520 nm
Spectral resolution (FWHM)	0.42 nm – 0.52 nm
Oversampling	8 pixels
Spectrometer slit width	50 μm
Grating line density	1200 mm^{-1}
Grating blaze wavelength	250 nm
CCD array size (pixels)	14 × 2048
CCD pixel size (μm)	25
80% full well S/N (1 sigma)	300:1
CCD dynamic range	16 bit
Minimum integration time	4 ms
FOV (sun and sky)	1.6°

Table 5.2 MFDOAS characteristics

Wavelength interval	282 nm – 498 nm
Spectral resolution (FWHM)	0.83 nm
Oversampling	7.8 pixels
Spectrometer slit width	100 μm
Grating line density	400 mm^{-1}
Grating blaze wavelength	400 nm
CCD array size (pixels)	512 × 2048
CCD pixel size (μm)	13.5 × 13.5
80% full well S/N (400 rows)	5640:1
CCD dynamic range	16 bit
Integration time	20 ms – 60 s
FOV (sun)	1.5°

FWHM) average spectral resolution. The wavelength coverage is from 282 nm to 498 nm. The CCD is thermoelectrically cooled to −70°C. Direct sunlight enters the instrument through a 25 cm black anodized, baffled snout with a quartz window for weather control. A biconvex lens focuses the sunlight onto an 8 cm spectralon integrating sphere that moves into the spectrometer's FOV during the direct-sun measurements. A series of baffles inside the telescope limit the direct-sun field of view to about 1.5°. The sky FOV is a narrow rectangle that is 1° wide. Use of an integrating sphere assures equal illumination of the optics and minimizes the effect of pointing errors, eliminating a critical source of spectral residual error. Light from the scattered sky or the direct sun passes through two filter wheels containing optional depolarizers, a spectral flattening filter, and UV-transmitting and UV-cutoff filters.

The two independently developed instruments have been compared during two

campaigns at GSFC and JPL's Table Mountain Facility in California (TMF) and found to agree very closely (Herman et al., 2009a). During these campaigns, both instruments measured $C(NO_2)$, the column amount of NO_2, in the atmosphere using direct-sun observations of atmospheric absorption. The precision achieved was 0.01 DU (1 DU $= 2.67 \times 10^{16}$ molecules/cm^2) with an accuracy of ± 0.05 DU compared to the minimum $C(NO_2)$ in the atmosphere of 0.1 DU. This level of precision and accuracy is sufficient to measure UV and VIS radiances, as well as trace gas amounts (O_3, SO_2, NO_2, H_2O and aerosols). The measured trace gas and aerosol amounts can be used to calculate UV irradiances and radiances over the entire 300 nm to 400 nm range.

The large dynamic intensity range as a function of wavelength can cause a well-known spectrometer system problem of stray light from longer wavelengths affecting the radiometric response of the shorter wavelengths. This problem is minimized by using bandpass filters (e.g., UV-340 filter) that block the visible and pass the UV so that ozone amounts can be measured (305 nm – 320 nm) by the same instrument that measures NO_2 (400 nm – 450 nm). The best performance is obtained by use of a double filter wheel with one wheel containing neutral density ND filters, open hole, and blocked hole, and the other containing function filters (e.g., UV-340, polarization filters, open hole etc.). The blocked hole is essential for the measurement of spectrometer dark current correction in between each measurement of radiance for the same exposure time as the radiance measurement. The use of fiber optic cables to connect the optical head to the spectrometer (Pandora) has advantages (modularity, light weight, depolarization, and remote operation) and disadvantages (radiometric stability, calibration, controlling the FOV, and some fragility) compared to direct coupling of the optical head to the spectrometer (MFDOAS). While these problems are not trivial, they have been mostly overcome.

For all of these instruments, the key factors are the absolute accuracy of the calibration and the long-term stability (precision) of the instrument. Absolute accuracy is achieved by measuring the output of a standard lamp that has been verified by an appropriate standards organization (e.g., the National Institute Standards and Technology (NIST), in the U.S., or one of the European standards laboratories). The quality of the transfer of calibration is dependent on a meticulous laboratory setup between the standard lamp and the instrument in question. Currently, the best transfer of calibration produces an accuracy of between 2% and 3% under the assumption that the instrument has been fully characterized in the laboratory before the use of a standard lamp (slit functions, filter transmission functions, wavelength calibration, temperature sensitivity, stray and scattered light, etc.). The achievable accuracy will be a combination of the instrument characterization errors and the lamp transfer radiometric calibration. Note: To determine the wavelength dependent slit functions over the entire wavelength range or the filter functions, the detector must have many light sensitive elements within the projection of the grating's spectral resolution onto the detector at its

full width at half the maximum height (FWHM) or the width of the filter bandpass at FWHM. For wavelength scanning spectrometers, the scanning step size must be much less than the spectral resolution FWHM to accurately determine the slit function.

Good long-term stability of the instrumentation is needed to detect possible changes in the amount of radiation reaching the ground. The stability can be determined by repeated checks against standard lamps in the laboratory or by techniques applied to the data obtained in the field. The most common of these is a procedure that attempts to derive the solar irradiance above the atmosphere by measuring solar irradiance at the ground as a function of SZA (Langley method). This gives a series of measured instrument counts as a function of the amount of atmosphere between the instrument and the sun. If the atmosphere is approximately stable over the period of the measurements, the series of measurements can be extrapolated back to zero atmospheres. The details of a modified Langley method are described in Herman et al. (2009a). Repeating this procedure frequently for the life of the instrument can give a measure of the instrument's stability or precision. The best Langley procedures are performed at extremely clean sites such as Mauna Loa, Hawaii, where the interference from changing aerosol and boundary layer ozone amounts is at a minimum. The combination of frequent standard lamp calibration and in the field Langley procedure provides a precision between 2% and 3%. Some instruments, such as a well-maintained double Brewer spectrometer, are known to be very stable against standard lamps and can produce a radiance precision near 1% if the instrument is modified to be polarization insensitive (Fig. 5.3(c)).

In addition to ground-based instruments, there have been several spectrometers located on satellites since 1979, which are able to provide accurate estimates of ozone and cloud transmission T (through measured cloud and aerosol Lambert Equivalent Reflectivity R (Herman et al., 2001a; 2009b; see Section 5.3.4), where T is approximately $1-R$). The estimate for T has been improved by detailed radiative transfer solutions for plane parallel clouds of different optical thickness. The resulting cloud transmission factor C_T (Krotkov et al., 1998) gives results that are close to the simple expression $C_T=(1-R)/(1-R_G)$, where R_G is the measured surface reflectivity and $R_G<R<1$ (Herman et al., 2001b). This expression for C_T has been given by Krotkov et al. (1998), and can be derived from a Stokes calculation (see Section 5.3.5) for a transmitting and reflecting surface over a reflecting ground (Herman et al., 2009b). Ultraviolet and VIS irradiance, at ground-level or within the atmosphere, can be accurately estimated using radiative transfer calculations that include the appropriate absorbing gases, aerosol scattering and absorption, surface reflectivity, and cloud transmission. Frequently, the calculated amount of radiation is overestimated by 10% to 20% because of the lack of knowledge regarding aerosol absorption, even when the aerosol optical depth is known, especially in urban areas (Herman et al., 1999).

Instrumental requirements for making long-term UV irradiance measurements

are well understood in terms of calibration and stability for both spectrometers and broadband radiometers (WMO, 1999; 2003; 2007). The degree to which further improvements are made to a given instrument type should be dictated by the scientific goals of an application. For example, different accuracy and precision are needed for estimating transmission through the atmosphere in the presence of trace absorbing gases, changes in UV and VIS radiances and irradiances needed for estimating changes in atmospheric chemistry photolysis rates, climate change studies, or for use in various applications (estimations of solar radiation amounts vs. cancer incidence, material damage, atmospheric photochemistry, and biological productivity).

Biological or material damage applications are usually expressed in terms of "action" spectra, which are an estimate of the relative strength of a given process (e.g., skin reddening) for a given wavelength per unit of incident solar radiation. The biological action spectra are usually poorly known and have a wide variation within a species depending on skin or surface type, genetics, species adaptation to its local environment, and from species to species. In other words, knowing the solar radiation change to within a few percent, or even 10%, is good enough for most biological and materials damage process studies. Of more importance is determining the changes in exposure to solar radiation either in the same location or by moving to lower latitudes where there is usually more solar irradiance.

Higher accuracy and precision are needed for understanding physical processes, such as contributions to atmospheric energy balance related to global warming or for estimations of photolysis rates for atmospheric chemistry studies. The estimated surface heat imbalance between the surface re-radiation and the atmosphere is about $+9$ watts/m^2 (Lin et al., 2008), so that a contribution of 1 watt/m^2 would be a significant portion of the uncertainty. For the UV range from 300 nm to 400 nm, there are approximately 100.7 watts/m^2 at the top of the atmosphere and about half that at the surface, so that detecting a 1-watt/m^2 change in the UV band over a decade would require 2% long-term precision.

5.3 Detection of Long-Term Change

Long-term ground-based UV spectral irradiance measurements must be carefully made and analyzed to preclude variations due to clouds that could be mixed into UV trend estimates, or whose variability can mask the detection of small changes. If ground-based data are filtered for cloud-free observations, then UV-B changes caused by the variability in ozone amounts are easily observed in multi-year data records. Aerosols and other forms of pollution can also produce apparent changes in UV irradiance that masks the effect of ozone changes. These changes can be taken into account if measurements are made simultaneously within the UV-B range (e.g., 305 nm) and outside of the ozone absorbing range (e.g., 324 nm). The lack of ability to separate aerosol and pollution effects from ozone-induced

changes limits the usefulness of broadband instruments (300 nm – 400 nm) for understanding the observed irradiance changes.

Radiometric and wavelength calibration of spectrometers used for irradiance trend estimates must be carefully maintained to detect the relatively small changes caused by ozone and aerosols. Making accurate spectral measurements can be difficult, since the natural UV spectrum at the ground changes by several orders of magnitude from 300 nm to 400 nm. A slight wavelength misalignment can cause significant errors in the measured UV-B irradiance amount. Wavelength misalignment is less important for broadband wavelength integrated quantities, such as erythemal irradiance. Equally difficult are measurements of UV irradiance ratios at both small (near noon) and large SZAs (near sunrise or sunset) because of the large dynamic range required. The use of sensitive CCD spectrometers and multiple neutral density filters can mitigate the intensity problem at the expense of some additional calibration. Experience to date with the backthinned CCD Pandora spectrometers indicates both the spectrometers and the optics are stable with field calibration and suited for both short- and long-term measurements.

5.3.1 Radiation Amplification Factor

An alternate method for the estimation of long-term changes in UV-B irradiance can be devised by combining measured ozone values with radiative transfer calculations. These calculations can be simplified for estimating irradiance change by neglecting scattering effects. For clear-sky, constant cloud, and constant aerosol conditions, changes in monochromatic UV-B irradiance dF show a well-defined inverse relation with changes in the amount of ozone dΩ in the atmosphere based on laboratory measurements of the ozone UV absorption coefficient α (e.g., Zerefos et al., 2001). This has been most clearly demonstrated using a spectroradiometer measuring ozone and erythemally weighted irradiance (300 nm – 400 nm) at Mauna Loa, Hawaii on 132 clear mornings between July 1995 and July 1996 (WMO report, 1999). The relationship of a change in irradiance dF at a single wavelength to a small change in column ozone amount dΩ is approximately given in Eq. (5.1).

$$\mathrm{d}F/F = -\mathrm{d}\Omega/\Omega\,\alpha\Omega\sec(\theta) = -\mathrm{d}\Omega/\Omega\,(\mathrm{RAF}) \tag{5.1}$$

The differential relationship is derived from the standard Beer's Law of irradiance F attenuation in an absorbing atmosphere, $F = F_o \exp(-\alpha\Omega \sec(\theta))$, where Ω = the ozone column amount in DU (1 DU = 1 milli-atm-cm or 2.69×10^{16} molecules/cm^2), α = the ozone absorption coefficient (in cm^{-1}), θ = the SZA, and F_o is the irradiance at the top of the atmosphere. The quantity $\alpha\Omega \sec(\theta)$ is the slant path optical depth, which was also named the Radiation Amplification Factor, or RAF(Ω,θ) (Madronich, 1993) when Eq. (5.1) was used for estimating irradiance change. When varying cloud reflectivity dR is included, $F = F_o \exp$

$(-\alpha\Omega\sec(\theta))\,(1-R)/(1-R_G)$ and the fractional change in irradiance is

$$dF/F = -d\Omega/\Omega\,\alpha\Omega\,\sec(\theta) + dC_T/C_T \tag{5.2}$$

where C_T = the cloud + aerosol transmission = $(1-R)/(1-R_G)$,
and R = the reflectivity of the ground R_G + cloud R_C system ($R_G < R < 1$).

Equation (5.2) has proven to be quite accurate for estimating monochromatic irradiance changes for small changes in Ω under a wide variety of conditions, especially for cloud-free conditions. A comparison was run between radiative transfer solutions RTS and Eq. (5.1) for 1% change from three ozone values, 275 DU, 375 DU, and 475 DU for the wavelength range 290 nm to 350 nm, and SZA = 30° (Herman et al., 1999). The largest difference between the RTS and Eq. (5.1) was 0.2% at 290 nm for 275 DU, and less than 0.1% for wavelengths larger than 310 nm.

Figure 5.5 shows a specific example of the cloud-free monochromatic RAF for $\Omega = 0.33$ atmosphere-cm = 330 DU and SZA = 45°, and shows the ozone absorption coefficient (cm^{-1}) for the wavelength range from 240 nm to 340 nm. The RAF method accurately estimates small monochromatic UV irradiance changes compared to clear-sky radiative transfer (Herman et al., 1999). For example, radiative transfer shows that a 1% decrease in O_3 produces a 2.115% increase in 305 nm irradiance, while the RAF method estimates a 2.064% increase ($\Omega = 375$ DU, $\theta = 30°$). There are wavelength dependent deviations from Eqs. (5.1) and (5.2) under optically thick clouds caused by multiple scattering increasing the optical path for ozone absorption. If there is a 1% change in ground reflectivity from a

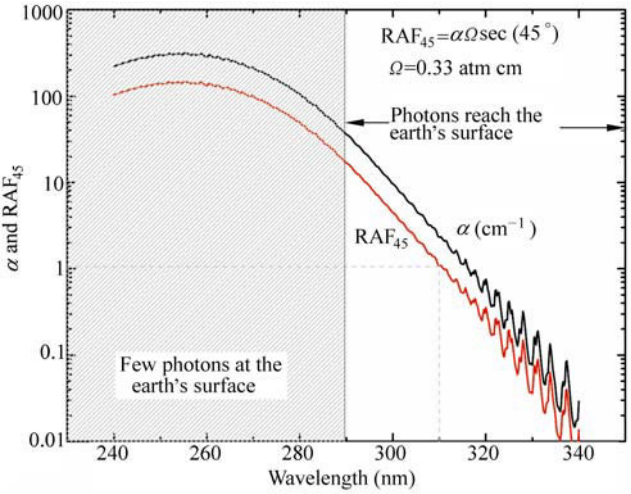

Figure 5.5 Ozone absorption coefficient α (cm^{-1}) and the RAF_{45} for an SZA = 45° and ozone amount of 330 DU ($\Omega = 0.330$ atm cm). Note that at 310 nm, the $RAF_{45} \sim 1$, so that a 1% increase in O_3 would produce a 1% decrease in 310 nm irradiance

nominal reflectivity of $R_G = 5$ RU ($R_G = 0.05$) for clear skies, the change in downward irradiance is less than 0.35% due to backscattering from the atmosphere. If there is optically thick cloud cover, the change increases to about 0.8%.

The RAF method has also been validated using measurements of ozone and UV irradiance at Mauna Loa, Hawaii. Figure 5.6 shows that when clear-sky measurements of monochromatic irradiance are carefully made for a 1% change in ozone amounts, but no change in aerosols, the measured and calculated changes agree quite well. Later, it is shown that an empirical power-law RAF method agrees with monochromatic Eq. (5.1) for small ozone changes, but also applies for action spectrum weighted irradiances with larger ozone changes. The empirical power law can be obtained (numerically) from Beer's Law (see Section 5.7).

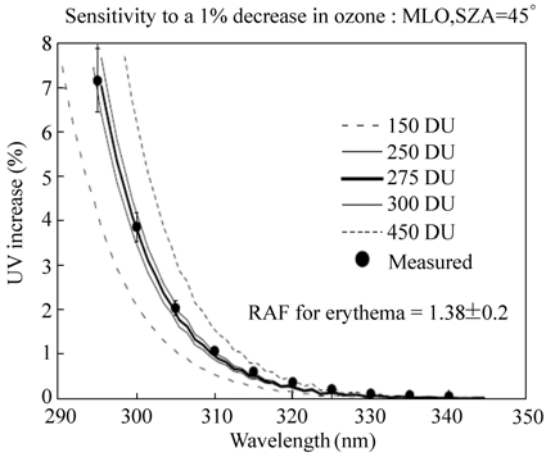

Figure 5.6 Validation of RAF method using the measured (dark circles) changes in ozone and UV irradiance from Mauna Loa, Hawaii (WMO, 1999)

Fioletov et al. (1997) reported an extensive analysis of UV-B irradiance and its dependence on total ozone. The analysis provides an empirical wavelength-by-wavelength measure of the increase of UV-B irradiance for a 1% decrease of total ozone. The values for UV change with ozone change were found to be essentially the same for clear and cloudy conditions (except for very heavy clouds), and are in good agreement with model results for longer wavelengths and moderate SZA. The conclusion is in agreement with the approximation in Eqs. (5.1) and (5.2).

Both theory and observations show that reductions in ozone lead to increases in UV erythemal and UV-B monochromatic radiation at the earth's surface. For mid-latitudes, changes in measured erythemal irradiance can be approximated using Eq. (5.1) with the monochromatic RAF = 1.3 to 1.4 at mid-latitudes when the ozone amount changes by 1%. However, an empirical power law form gives a better approximation to erythemal irradiance change with ozone than Eq. (5.1). A detailed discussion of RAF is given in Section 5.7.

Satellite estimates of ozone and reflectivity are retrieved separately, each with its own error budget. Ozone is retrieved with about 1% accuracy, especially on a zonal average basis. Zonal average reflectivity is retrieved with an accuracy of about 2 RU or 0.02 ($0 < R < 1$). The differences $d\Omega$ and dR have the same accuracy as Ω and R, since they are simply the difference from a fixed reference value. When Eqs. (5.1) and (5.2) are used for estimating UV trends in this study (see Section 5.3.7), the reference values used are the average value of ozone or reflectivity in the first year as a function of latitude.

The implication of this and following sections is that it may be easier to measure changes in ozone amounts and cloud plus aerosol transmission combined with radiative transfer calculations of UV irradiance change than it is to measure the changes in UV irradiance with very stable and well-calibrated instrumentation. This method will miss some features of UV irradiance, such as the momentary increase above clear sky amounts caused by reflections from the sides of clouds and will not be accurate in mountainous regions where the terrain reflectivity affects the irradiance more than in relatively flat regions. Even in mountainous regions, Eq. (5.2) will still represent the change in irradiance caused by satellite-detected changes in stratospheric and tropospheric ozone amounts. However, changes in scene reflectivity from the sides of mountains can affect the amount of UV irradiance in a manner that is usually not detected by ozone-measuring satellites. The method will also miss any absorption effects (usually small) caused by other trace gases (e.g., NO_2 and SO_2) and absorbing aerosols. Currently there are no long-term measurements of these quantities and their changes over wide areas.

5.3.2 Different Definitions of RAF

An alternate power-law form for estimating action spectrum weighted irradiance change is commonly used for large changes in ozone amount, which empirically matches data quite well (Booth and Madronich, 1994; Blumthaler et al., 1995). This form is given in Eq. (5.3).

$$F_1/F_2 = (\Omega_1/\Omega_2)^{-\mathrm{RAF}(\theta)} \tag{5.3}$$

where Ω_1 and Ω_2 are two values of ozone that correspond to two values of irradiance, F_1 and F_2, respectively. The RAF(θ) is an empirically selected set of constants to match Eq. (5.3) to observed data. For small changes in Ω, equation (5.3) is approximately the same as Eq. (5.1) by expanding $F_1/F_2 = [1 + (\Omega_1 - \Omega_2)/\Omega_2)]^{-\mathrm{RAF}} = 1 - \mathrm{RAF}\ [(\Omega_1 - \Omega_2)/\Omega_2)] + \cdots$, so that $(F_1 - F_2)/F_2 = -\mathrm{RAF}\ (\Omega_1 - \Omega_2)/\Omega_2 + \cdots$ for $(\Omega_1 - \Omega_2) << \Omega_2$.

The primary use for the power-law form is for processes that span a wide wavelength range that includes UV-B and UV-A. The best-known example is the erythemal action spectrum weighted irradiance $A_{\mathrm{ERY}}(\lambda)F(\lambda)$, where the weighting is given by the McKinlay and Diffey (1987) action spectrum $A_{\mathrm{ERY}}(\lambda)$ (see

Section 5.7). Since the power law form is empirical, measurements or radiative transfer calculations, as a function of ozone amount, must be made to estimate $RAF_{ERY}(\theta)$. For large SZAs the UV-B portion of the irradiance diminishes rapidly and the product $A_{ERY}(\lambda)F(\lambda)$ is dominated by UV-A, which has almost no sensitivity to ozone change. As a function of latitude, the mid-day $RAF_{ERY}(\theta)$ is approximately constant in low and middle latitudes, and then decreases at high latitudes (high SZA) (Bodhaine et al., 1997). This behavior appears to be quite different from the monochromatic RAF in Eq. (5.1) (see Section 5.7).

The existence of two definitions of RAF (Beer's Law, equation (5.1) and Power Law, Eq. (5.3)) can cause some confusion. The physically based Beer's Law formulation can also be used to derive monochromatic $\Delta F/F$ for large changes in ozone $\Delta\Omega/\Omega$. Let $F_1 = F_0 \exp(-\alpha\Omega_1 \sec(\theta))$ and $F_2 = F_0 \exp(-\alpha\Omega_2 \sec(\theta))$, then define $\Delta F_{12}/F_2 = (F_1 - F_2)/F_2$ and $\Delta\Omega_{12}/\Omega_2 = (\Omega_1 - \Omega_2)/\Omega_2$. The result is given in Eq. (5.4).

$$\Delta F_{12}/F_2 = \exp(-\alpha\Omega_2 \sec(\theta)\, \Delta\Omega_{12}/\Omega_2) - 1 \tag{5.4}$$

In Section 5.7, we show that the use of Eq. (5.4) Beer's Law leads directly to the Power Law after integrating over the wavelength range corresponding to an action spectrum. In the following sections, $\Delta\Omega_{12}/\Omega_2$ is small, so that the change for near-monochromatic dF/F can be estimated from Eq. (5.1) or (5.4).

5.3.3 Estimating UV Trends: Discussion

Satellite observations of UV and VIS irradiance can be used to distinguish regional and global changes in derived atmospheric properties (e.g., ozone, sulfur dioxide, reflectivity, aerosol distribution, nitrogen dioxide, UV-irradiance) in contrast to purely local observations from ground-based instruments. The estimates are based on a single well-calibrated instrument that is used over extended periods (Herman et al., 1991; Herman et al., 1996). For example, the $\pm 52^\circ$ side scanning Nimbus-7/TOMS measured six radiance channels (312, 317, 331, 340, 360, and 380 nm, 1-nm wide) producing a full global map in each channel once per day for the period October 1978 to January 1993. As with most satellite instruments, the accuracy and precision were maintained using in-flight earth radiance and solar irradiance data to detect and correct changes from the pre-launch laboratory calibration. The data series obtained by Nimbus-7/TOMS has been extended through the present (2009) using the NOAA SBUV-2 series of spectrometers and the hyperspectral spectrometer OMI (270 nm – 500 nm with a resolution of about 0.5 nm).

Satellite derived geophysical quantities (column ozone amounts, values of aerosol optical depth, scene reflectivities (cloud, aerosol, plus ground), and a ground reflectivity climatology) are used to estimate the solar UV irradiance at the ground. Since the entire process is based on remote sensing, complicated retrieval

algorithms, and radiative transfer model calculations, the results must be validated against a small set of well-calibrated ground-based measurements distributed in a variety of regions that observe under different atmospheric and geographic conditions. The main purpose of these validation measurements is to provide timely warning that either the satellite or the ground-based instruments are experiencing calibration drift, or that there is some missing physical parameter in the satellite algorithm that can only be supplied from ground-based ancillary data (e.g., aerosol absorption).

UV radiation reaching the earth's surface varies on all time scales, from seconds to seasons to years. In today's atmosphere, the multi-year UV-B variations are principally controlled by changes in stratospheric ozone, changes in the extent of cloud cover, and other longer-term changes such as in the amount of aerosol and pollution. Day-to-day ozone-caused changes from stratospheric and tropospheric dynamics can be significant, but are usually smaller than changes due to cloud cover, because the stratospheric abundance of ozone usually changes as a moderate percentage (~15%) of its seasonally changing mean value. The broad, seasonally repeatable cloud patterns can also cause changes in daily and monthly time scales as the weather changes. On longer time scales (decadal), most regional changes in cloud cover have been small (Herman et al., 2009b), so that global and zonal average changes in UV-B due to long-term ozone depletion are dominant over cloud-change effects. In some regions (e.g., northern Europe), decadal-term cloud changes are also important. Ultraviolet-A changes are controlled by all of the above factors, except ozone.

Ozone data from Nimbus-7/TOMS, obtained during June for the entire 5° longitudinal zone centered at 40°N, shows that the day-to-day ozone amount can vary by 50 DU, the approximate mean value of 350 DU, or $\mathrm{d}\Omega/\Omega = \pm 0.14$. The day-to-day June ozone variation is obtained from figures similar to those shown in Herman et al. (1995). Using an average noon SZA for June of about 23° and an ozone absorption coefficient for 305 nm $\alpha = 4.75\ \mathrm{cm}^{-1}$ yields a typical 305 nm irradiance change $\mathrm{d}F/F = -\mathrm{d}\Omega/\Omega\,\alpha\Omega\sec(\theta) = \pm 0.14 \times 4.75 \times 0.35 \times 1.09 = \pm 0.25$. In other words, for clear-sky conditions, the 305 nm irradiance typically varies by ±25% during June, just from to day-to-day ozone changes. As will be discussed later, the day-to-day variability of clear-sky 40°N UV June irradiance is much larger than the change caused by the long-term June decreases in ozone from 1979 to 2008.

Other factors, such as Rayleigh scattering and land/ocean surface reflectivity, affect the magnitude of measured or theoretically estimated UV irradiance. However, these factors do not significantly affect the short- or long-term changes in irradiance, since their changes are small. Hourly or daily changes in Rayleigh scattering follow the small changes in atmospheric pressure, which usually are less than 2%. There have been no long-term changes in mean atmospheric pressure. The UV surface reflectivity R_G is small (3 RU − 10 RU) and almost constant with time, except in regions seasonally or permanently covered with snow or ice. Based on radiative

transfer studies, clear-sky atmospheric backscattering to the surface contributes less than 0.2 R_G to the measured UV irradiance, which is quite small for most ice/snow-free scenes (Herman et al., 1999).

5.3.4 Reduction of UV Irradiance by Clouds and Aerosols

A measured daily cycle of UV reaching the surface will show large UV irradiance reductions from clear-sky conditions as clouds pass over a site while blocking the view of the sun. These reductions are frequently in excess of those caused by measured ozone changes from climatological values for wavelengths longer than 305 nm. In general, the effect of clouds and aerosols reduces the UV and VIS amounts at all wavelengths reaching the earth's surface. When using satellite data to estimate the amount of UV reaching the surface, the average amount of UV radiation reduction caused by clouds, plus scattering aerosols, can be estimated from the Lambert Equivalent scene Reflectivity (LER), which varies significantly between locations on the coarse resolution scale of the satellite instrument (50 km to 100 km). The cloud reflectivity estimation can only be done for snow and ice-free conditions,

The LER of a scene is calculated by requiring that the measured radiance I_{SM} match the calculated radiance I_S at the observing position of the satellite by adjusting a single free parameter R in the formal solution of the radiative transfer equation in Eq. (5.5).

$$I_S(\Omega,\Theta,R,P_O) = \frac{RI_d(\Omega,\Theta,P_O)f(\Omega,\Theta,P_O)}{1-RS_b(\Omega,P_O)} + I_{dO}(\Omega,\Theta,P_O) = I_{SM} \qquad (5.5)$$

Ω = column ozone amount
Θ = viewing geometry (SZA, satellite look angle, azimuth angle)
R = LER at P_O, $0 < R < 1$
P_O = pressure of the reflecting surface (e.g., ground or cloud)
S_b = fraction scattered back to P_O from the atmosphere
I_d = sum of direct and diffuse irradiance reaching P_O
f = fraction of radiation reflected from P_O reaching the satellite
I_{dO} = radiance scattered back from the atmosphere for $R = R_G = 0$ at $P = P_O$

The quantities S_b, I_d, f, and I_{dO} are calculated from a radiative transfer solution and stored in tables. From Eq. (5.5),

$$R = \frac{I_{SM} - I_{dO}}{I_d f + (I_{SM} - I_{dO})S_b} \qquad (5.6)$$

The quantities in Eq. (5.6) are calculated from the TOMRAD vector radiative transfer program for a pure Rayleigh atmosphere for different values of R and P_O to create a table lookup capability. The details of the implementation are given in

the paper written by Dave (1964) from which TOMRAD was developed. Essentially, the quantities S_b and f are calculated for unit upward irradiance leaving the surface at P_O. In the case of S_b, it is the fraction that scatters back to the surface, and in the case of f, it is the fraction that reaches the satellite. I_{dO} is computed for the case $R_g = 0$.

The earth's reflectivity as represented by the LER is not the same as the angularly dependent reflectivity of a surface containing structures (grass, vegetation, mountains, clouds, etc.). The angular effects caused by structures in the surface and in clouds are minimized by scene averaging from the coarse resolution of the observations. In order to use the LER to estimate change in reflectivity, the observing geometry must be approximately constant over the life of the satellite, or corrections must be made to account for the change in angular dependence of the observations. Most of the satellites used to construct the reflectivity time series were in near-noon sun-synchronous orbits. This means that any location on the earth's surface was observed at approximately the same angle for the same day of each year. Long-term changes in LER represent changes in the scene reflectivity (clouds, aerosols, and surface) for each location. Comparisons of LER between seasons contain an angular effect caused by the seasonal change in the noontime SZA from the changing solar declination angle $\pm 23.3^\circ$.

The Nimbus-7/TOMS instrument obtained daily global coverage for ozone and LER for over 13 years at a spatial resolution that varied between 50×50 km^2 to 100×100 km^2. For any given location on the earth's surface, frequency of occurrence histograms were constructed from satellite derived reflectivity values (Fig. 5.7) (Herman et al., 2001b). These histograms showed that the most commonly occurring values of R were about 3 RU − 5 RU greater than the surface reflectivity, and represent haze or very sparse cloud cover. Central Europe, represented by Germany, is quite different from North American sites in that the most frequent values are around 10 RU (127 days; 3.9%) or around 50 RU (128 days; 3.9%), with almost the same number of days (80 to 128 days; 2.4% to 3.9%) having 10 RU to 70 RU. Greenland is another extreme, where the reflectivity is always high because of the ice cover. Nevada and Virginia are similar, except that Nevada has a lower average reflectivity representing less cloud cover. Another extreme case is represented by Australia, where the average reflectivity (due to cloud cover) is very low, and cumulative UV exposure is high compared to the same latitude in the U.S.

Satellite observations of reflected UV indicate that reflectivities for typical mid-latitude cloud covered scenes have a wide range of values, which can reach 90 RU over high altitude cloud tops, which most frequently occurs in the tropics. Under snow-free conditions, the surface reflectivity R_G is usually between 2 RU and 4 RU, reaching about 10 RU in the Libyan Desert and similar small areas (e.g., Andes Mountain high deserts). Area-averaged clear-sky UV surface irradiance is then approximately reduced as a linear function of the cloud plus aerosol reflectivity, which can be written in terms of effective transmission. The cloud transmission is approximately given by $C_T = (1 - R)/(1 - R_G)$, where $R_G < R < 1$.

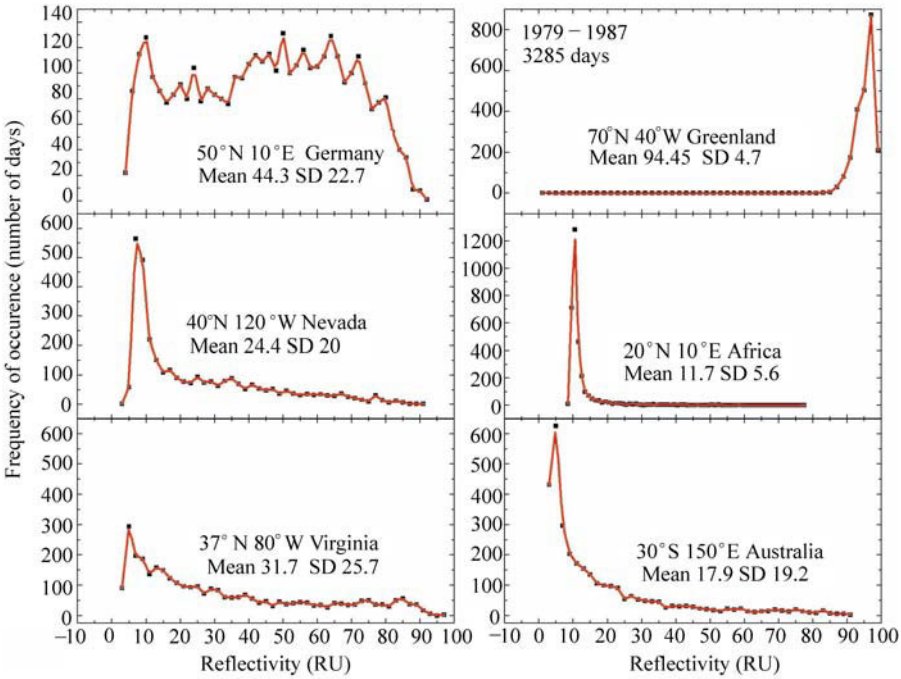

Figure 5.7 Frequency of occurrence of reflectivity values 1979 – 1987 (3285 days) for six different locations. The mean and standard deviation (SD) are in RU (1 RU = 1%). Based on Herman et al. (2001b)

5.3.5 Stokes Derivation of $C_T=(1-R)/(1-R_G)$

A satellite viewing the earth's surface observes a combined reflectivity $R=R_{SYSTEM}$ from the clouds and the ground. Assume that the cloud-ground system can be approximated by a two-layer Stokes problem with atmospheric effects neglected. Assume that the clouds have different transmission and reflections properties for diffuse T_D, R_D and direct-sun T_C, R_C. The arrows in Fig. 5.8 represent the partial contributions to the upward and downward fluxes.

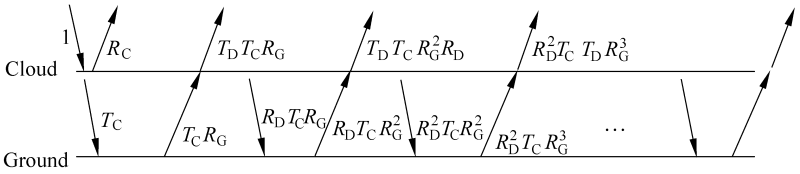

Figure 5.8 Stokes diagram for C_T for unit irradiance incident on a cloud of transmittance T_C over a surface of reflectance R_G. The cloud and surface have diffuse transmittance and reflectivity of T_D and R_D

$$R_{SYSTEM} = R_C + R_G T_C T_D \left[1 + R_G R_D + (R_G R_D)^2 + \cdots\right]$$

$$= R_C + R_G T_D T_C / (1 - R_G R_D) \tag{5.7}$$

$$C_T = T_C \left[1 + R_G R_D + (R_G R_D)^2 + \cdots\right] = T_C / (1 - R_G R_D) \tag{5.8}$$

Using Eq. (5.8), rewrite Eq. (5.7) as

$$1 - R_{SYSTEM} = 1 - R_C - R_G T_D T_C / (1 - R_G R_D) = 1 - R_C - R_G T_D C_T \tag{5.9}$$

Assume $T_C = 1 - R_C$ and $T_D = 1 - R_D$, rewrite (5.8) as $C_T (1 - R_G R_D) = 1 - R_C$.

Now Eq. (5.9) becomes $1 - R_{SYSTEM} = C_T (1 - R_G R_D) - R_G C_T (1 - R_D)$

$$= C_T (1 - R_G) \tag{5.10}$$

Finally, $C_T = (1 - R_{SYSTEM})/(1 - R_G)$ (5.11)

where

R_G = Reflectivity of the ground

R_C = Direct beam cloud reflectivity

R_D = Diffuse flux cloud reflectivity

R_{SYSTEM} = Reflectivity of the combined ground-cloud system

T_C and T_D are the corresponding cloud transmissivities

Assume $R = R_{SYSTEM}$ as an approximation of the reflectivity seen by the satellite

A problem exists for high reflectivity scenes observed by UV/VIS satellite instruments, such as those covered by snow or ice. Snow/ice covered scenes cannot be distinguished from cloud cover by radiance observations in the UV wavelengths. Because of this, the use of C_T to estimate the amount of UV radiation at the surface in the presence of snow is likely to be in error. For example, the very high reflectivity values observed in Greenland (Fig. 5.7) are almost independent of the cloud cover. Radiative transfer solutions for clouds over snow/ice surfaces show that the maximum reflectivity is obtained for clear-sky scenes, which is reduced somewhat in the presence of clouds over snow/ice (Krotkov et al., 1998).

Long-term changes in regional cloud and aerosol reflectivity must be considered when estimating long-term changes in UV irradiance. However, for most populated regions of the earth, long-term (decadal) cloud and aerosol scattering changes have been shown to be small, even where they are statistically significant (Herman et al., 2001a; Herman et al., 2009b). Local values of aerosol amounts and absorption are currently estimated from the widely distributed AERONET network of ground-based sunphotometers (Holben et al., 2001), and for clear-sky scenes, from satellite data (Torres et al., 2002a, b).

5.3.6 UV Absorption

The amount of UV radiation reaching the earth's surface is affected by air pollution, i.e., absorption by aerosols (black carbon, dust, and smoke), tropospheric O_3, NO_2, and other gases. These can cause typical reductions in UV radiation by up to 15% in polluted sites, but with much higher reductions occurring in certain highly polluted cities, e.g., occasionally in Los Angeles and frequently in Beijing. NO_2 causes small reductions, mainly to UV-A, since its absorption cross-section peaks near 410 nm, yet is still significant at 330 nm. Aerosols of most types affect UV and VIS radiation at all wavelengths. Pollution abatement, especially in highly polluted regions, can decrease the atmospheric reflectivity and absorption, which has the effect of increasing the amount of UV and VIS radiation reaching the ground. The reductions in surface UV can be much higher in regions affected by smoke (e.g., biomass burning) or by the major dust storms that frequently occur in Africa and parts of China.

Absorption of UV and VIS irradiance/radiance is used to determine the amount of pollution (O_3, SO_2, HCHO, NO_2, H_2O) in the atmosphere by matching the measured and calculated spectrum reaching ground-based spectrometers or reflected back to a satellite spectrometer (e.g., OMI and GOME) (Cede et al., 2006; Wenig et al., 2006).

5.3.7 Estimating Zonal Average UV Change

Since changes in cloud, plus aerosol, reflectivity have been small over the 1979 to 2008 period, except in some local regions (Herman et al., 2009b), the zonal average change in UVB radiation is dominated by changes in ozone amounts. For this purpose, the changes can be estimated from Eq. (5.1) or (5.3), or including the observed LER change term as in Eq. (5.2). The ozone data set is based on a combination of satellite data from Nimbus-7/TOMS, the SBUV-2 series of satellite data, EP/TOMS, and AURA/OMI organized into monthly average and zonal average time series. The time of the day is taken as local noon, so that the SZA is the latitude $L \pm \delta$ (the solar declination angle δ) depending on the day of the year T. When $t = 12$ (noon), $\mathrm{SZA} = L - \delta$ from Eq. (5.12).

$$\cos(\mathrm{SZA}) = \cos(L)\cos(\delta)\cos[\pi(t-12)/12] + \sin(L)\sin(\delta) \tag{5.12}$$

A useful, but moderate, accuracy estimate for δ (degrees) as a function of the day of the year T (days from 1 to 365) is given in Eq. (5.13). Knowledge of SZA is needed to evaluate Eqs. (5.1) to (5.4) to estimate UV or VIS changes from satellite data discussed in Section 5.3.8.

$$\delta = \frac{180}{\pi}\arcsin\left[c\cos(\theta + d)\right] \tag{5.13}$$

$\theta = 0.5a(2+b^2)T + 2ab\sin(T) + 0.25ab^2\sin(2T)$
$a = 0.017{,}202{,}166$
$b = 0.016{,}75$
$c = -0.397{,}68$
$d = 0.177{,}84$

5.3.8 Estimating UV Trends: Satellites

Global estimates of surface UV irradiance F_λ as a function of latitude, longitude, and wavelength λ have been calculated from satellite measurements of atmospheric backscattered UV radiances and the small amount reflected from the surface. The long-term precision and stability of a satellite instrument's in-flight calibration, especially the single-channel radiances used to estimate cloud transmission and reflectivity, make it very useful for estimating trends in F_λ. In the absence of a widely distributed, closely-spaced surface network of well-calibrated UV spectrometers, satellite UV irradiance estimates are extremely useful, especially over ocean areas where there are no other measurements.

There are two ways of estimating the UV irradiance reaching the ground from satellite remote sensing of ozone, aerosol, and reflectivity. First, one can enter these quantities into a detailed radiative transfer model to compute cloud transmission C_T using Mie theory to approximate the cloud and aerosol properties, in addition to Rayleigh scattering and ozone absorption (Krotkov et al., 1998; 2001). The second approximate method, is to estimate the irradiance reaching the ground for a Rayleigh scattering and ozone absorbing atmosphere F_{CLEAR}, and then add the cloud and aerosol transmission as a correction factor based on the measured fractional scene $R\,(0<R<1)$ and surface reflectivity R_G, $T \approx (1-R)/(1-R_G)$, where $0<T<1$. The irradiance at the surface is then approximately

$$F_{SURFACE} = T\,F_{CLEAR} \tag{5.14}$$

The two methods quite closely agree (Krotkov et al., 2001), except when there is enough multiple scattering within a cloud to give enhanced ozone absorption at wavelengths less than about 310 nm where C_T is the better estimate. Irradiances from both the C_T and the simplified methods are frequently higher than measured irradiance values on the ground, usually caused by an underestimate in the satellite calculation of aerosol amounts and aerosol absorption (Krotkov et al., 1998; 2001; Herman et al., 1999; Kalliskota, 2000). The differences become much less when the aerosol amount is small or is known from ground-based measurements. Other sources of differences between ground-based measurements and satellite estimates of UV irradiance arise from the large satellite field of view (50×50 km^2 at nadir for TOMS and 13×24 km^2 for OMI) compared to the smaller ground-based field of view, in addition to the terrain height differences within a satellite field of view.

A recent comparison of measured UV erythemal irradiance from ground-based measurements and OMI satellite estimates has been made (Tanskanen et al., 2007). The comparison shows that for flat, snow-free regions with modest loadings of absorbing aerosols or trace gases, the OMI-derived daily erythemal doses have a median overestimation of 0% to 10%, and that 60% to 80% of the satellite estimated erythemal doses are within ±20% compared to ground-based measurements.

Similar errors occur when interpolating between widely separated ground-based stations, where the aerosol, ozone, and cloud amounts vary between the stations. Given the need for global coverage of F_λ, and the sparsely located ground-based stations, calculations of F_λ from satellite-observed column ozone abundances and cloud reflectivities, which are validated by ground-based measurements, are a useful method for estimating regional, zonal averages, and global UV irradiance trends.

The year-to-year shifts in cyclic weather patterns (e.g., clouds, ozone transport, etc.) by even a tenth of a degree in latitude and longitude (~10 km), strongly affect ground-based UV measurements and their estimates of UV irradiance trends, but have a minimal effect on area-averaged satellite ozone and reflectivity measurements (and the UV estimates derived from them). Therefore, the surface UV changes deduced from ozone amounts and reflectivity measured by satellites, F_λ, are expected to be equivalent to those from cloud-filtered, ground-based observations of UV irradiance, and are superior for estimating regional and global changes. Satellite measurements provide both regional and global long-term coverage, which can be used to construct zonal and regional averages and long-term trends, which have much less geophysical variance from clouds than corresponding ground-based measurements. However, most satellite measurements are from low earth polar orbits that pass over a given site only once a day, and so represent the precise cloud conditions for that local time (usually from 10:30 to 13:30 hours), which misses the morning to afternoon variation. For the purposes of UV trends, the estimations are usually calculated for solar noon geometry using ozone amount and cloud reflectivity from sun-synchronous satellite near-noon measurements.

The use of satellite estimates presupposes ground-based measurements for validation and as a bridge between successive satellite instruments, if there are gaps. However, the determination of local UV irradiance is best achieved by ground-based measurements of either the irradiance or the atmospheric properties (ozone, aerosols, and clouds) above the observation site from which the irradiance can be calculated.

Satellite-observed long-term changes in mid-latitude zonal average ozone amounts suggest that there were significant UV increases for both erythemal irradiance and individual UV-B F_λ. The zonal average irradiance increase, relative to 1980, for the latitude band between 30°N and 40°N peaked in 1993 at about 20% (erythemal irradiance) and 40% (305 nm irradiance). Fortunately, these increased percentage changes occurred during the winter months when the SZAs are large, so that the absolute irradiances were comparatively small and the biological effects

were minimal. The calculated annual average irradiance increase during 1993 was about 7% and 14%, for erythemal and 305 nm irradiances, respectively. By 2007, ozone had partially recovered so that the irradiance increase moderated to 4% and 8%, respectively. Model calculations show that the recovery is a direct consequence of the implementation of the Montreal Protocol, and its subsequent amendments, limiting the introduction of ozone destroying substances into the atmosphere.

The long-term (30-year) monthly and zonal average (5° bands) ozone time series can be used to estimate changes in monochromatic irradiance reaching the earth's surface using the RAF from Eqs. (5.1) and (5.2), and the estimate of the SZA as a function of latitude and season from Eqs. (5.12) and (5.13). Sample results are shown in Fig. 5.9 for latitude bands centered on 32.5°S and 32.5°N where the ozone change dO_3/O_3 is approximately −3% over 30 years. Since there has been no significant change in zonal average cloud cover (Herman et al., 2009b) at these latitudes, the increase in 305 nm irradiance dF/F is about 6% over 30 years for the summer months centered on June (Herman, 2009). While this increase is significant, it appears that the decrease in ozone and increase in irradiance has leveled off starting in the late 1990s.

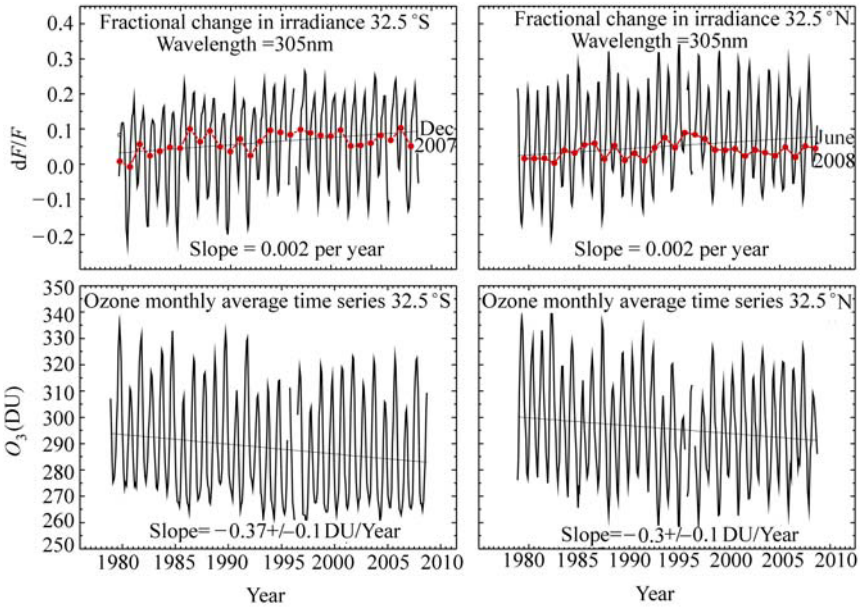

Figure 5.9 Fractional change in 305 nm irradiance dF/F (upper panels) caused by a change in ozone (lower panels) in two latitude bands centered on 32.5°S and 32.5°N of 5° width. The red dots represent the summer solstice months of December (−32.5°S) and June (32.5°N). The monthly average ozone values are available from the GSFC website based on merged data from multiple satellites (http://hyperion.gsfc.nasa.gov/Data_services/merged/index.html)

The two principal causes for change in irradiance at the earth's surface, dO_3/O_3 and dR/R are shown in Figs. 5.10 and 5.11. The change in reflectivity is based on the preliminary analysis of reflectivity (Herman et al., 2009b; Herman, 2009) for the entire 1979 to 2008 period. The current best-calibrated nadir-view zonal averaged LER values are averaged values from the temporally overlapping satellites listed in Table 5.3. The final numbers are expected to be slightly different than those in Fig. 5.11, so that the cloud-transmission correction to the 305 nm irradiance caused by variability in cloud cover will also change in the final analysis.

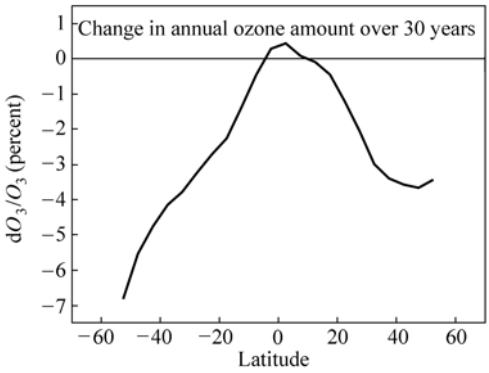

Figure 5.10 The 30-year percent change in zonal average annual ozone amount as a function of latitude

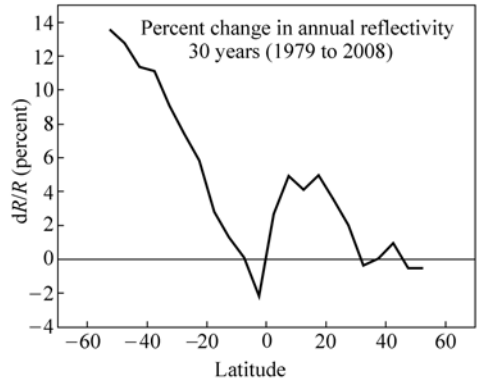

Figure 5.11 The 30-year percent change in zonal average annual reflectivity caused by clouds and aerosols (preliminary estimate)

Based on these numbers, an analysis for the annual mean change of 305 nm irradiance can be carried out for multiple latitudes with the results shown in Fig. 5.12. The changes in 305 nm irradiance are quite large at higher latitudes in both hemispheres, but especially in the Southern Hemisphere where it amounts to an

Table 5.3 Satellite instruments for ozone and reflectivity

1979 – 1992	Nimbus-7/TOMS (N7)	Full global coverage every day. Only a few missing days from1980 to 1992. Ozone plus reflectivity. Near noon orbit
1985 – 2008	SBUV-2 Series (N-9, N-11, N-16, N-17, N-18)	Nadir viewing only. Only a few missing days. Ozone plus reflectivity. N-9 and N-11 have a drifting orbit
2004 – 2008	Ozone Monitoring Instrument (OMI)	Full global coverage every day with few missing days. OMI produces both ozone and reflectivity values. 1:30 p.m. orbit

approximate 13% increase at 50°S latitude near the southern tip of South America. As shown in Fig. 5.12, the percent change in irradiance is dominated by changes in ozone amounts, except near the equator where the change in C_T dominates. The apparent leveling off with latitude of ozone change between 35°N and 50°N does not appear as strongly in the irradiance change because of the sec(θ) term in the expression for dF_{12}/F_2. The increase in cloudiness (decrease in C_T) at high southern latitudes moderates the irradiance increases caused by ozone decreases. While these estimated irradiance changes are significant, they are caused by small changes in ozone amount compared to the mean ozone value, which would permit the use of Eqs. (5.1) and (5.2), or the more accurate direct use of Beer's Law (Eq. (5.4)) as shown in Fig. 5.12.

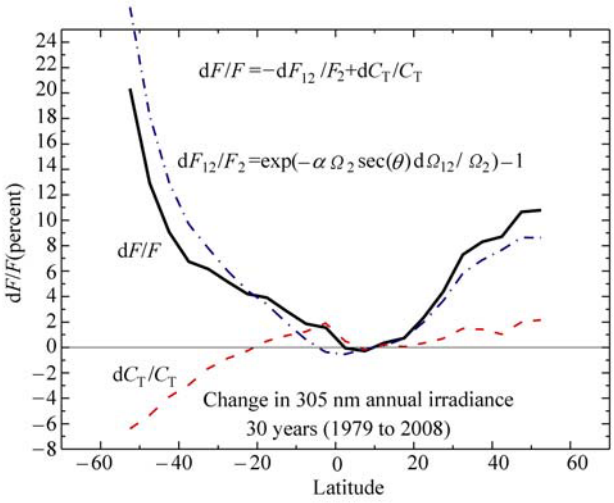

Figure 5.12 The annual average change in annual 305 nm irradiance (solid line) caused by changes (preliminary) in reflectivity and cloud transmission C_T (dashed line) and the change in ozone amount Ω (dot-dash line)

5.3.9 Estimating UV Trends: Ground-Based

An excellent example of UV trend detection is from ground-based measured solar irradiances at 305 nm and 324 nm at Thessaloniki, Greece. The irradiances shown in Fig. 5.13 are for cloud-free skies at a constant SZA of 63° (WMO, 2007, an extension of Bias et al., 1993). These data are obtained from a carefully maintained Brewer spectrometer located in an industrial area that is subjected to moderate amounts of pollution generated locally and also reaching Greece from other countries in Europe. There are also occasional dust episodes originating in northern Africa.

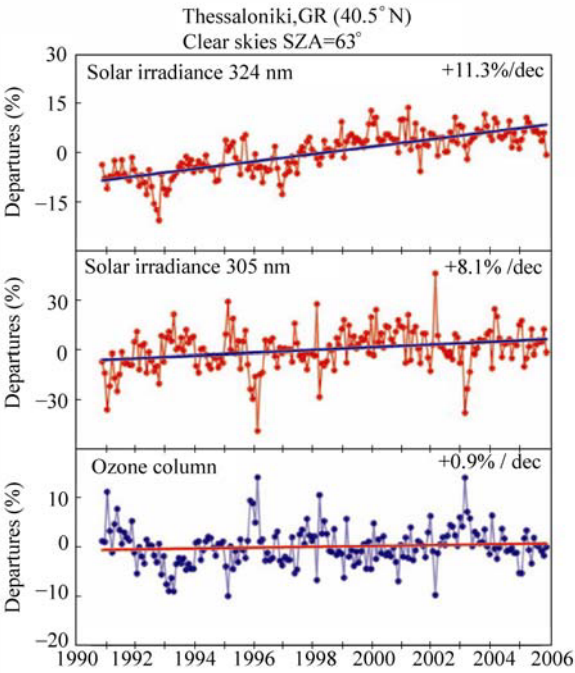

Figure 5.13 Combined effects of ozone, aerosols, and other absorbing components on UV radiation. Long-term variability in monthly mean solar spectral irradiances at 324 nm (upper panel) and at 305 nm (middle panel) measured at Thessaloniki, Greece, under clear skies at 63° SZA, shown as departures from the long-term (1990 – 2006) averages. The lower panel shows the corresponding departures in the ozone column of 375 DU (from WMO, 2007)

The radiation at 324 nm should not be significantly affected by ozone so that the cause of the upward trend at 324 nm (11.3% per decade) is almost certainly due to aerosol and pollution decreases. Decreasing amounts of aerosol and pollution that cause the upward trend at 324 nm will also affect 305 nm by approximately

the same amount. Combining the changes seen for 324 nm with those observed for 305 nm (8.1% per decade) implies that the effect of increasing ozone amounts (0.9% per decade) on 305 nm irradiance is a statistically significant decrease of $\sim(11.3-8.1)\% = 3.2\%$ per decade.

An easy way to check this conclusion is through the RAF defined as part of Eq. (5.1); $\mathrm{RAF} = -\alpha\Omega\sec(\theta) = -4$ for $\Omega = 375$ DU, and $\theta = 63^\circ$, the average measured values for Thessaloniki. Based on the RAF and the observed ozone change of 0.9% per decade, the change in 305 nm UV irradiance $dF/F = \mathrm{RAF}\, d\Omega/\Omega$ should be $\sim -4(0.9)\% = -3.6\%$ per decade, consistent with the measurements of −3.2% and −3.4% per decade discussed above. In addition to the smaller ozone effects, Fig. 5.13 shows that a decline in air pollutants can cause increases in surface UV irradiance of 11.3% per decade in a local industrial site, such as Thessaloniki, Greece.

When data from cloudy and clear days are present in the UV time series, the measured trends in UV radiation at individual stations can have sufficient variation (typically 0% − 50%, and occasionally larger due to cloud cover) to make estimated long-term trends lose statistical significance. As shown in a report by WMO (2007), trend estimates for Toronto for the period of 1998 through 2005 were $(1.5 \pm 5)\%$ per decade (1 standard deviation, 1σ) (WMO, 2007) during a period in which the total ozone amount was relatively constant. Even using unfiltered Toronto UV radiation data going back to 1990, no statistically significant trend is observable in the extended Toronto UV data despite ozone decreases that took place during the 1990s, due to the variability introduced by clouds. To relate the estimated trends to ozone changes requires knowledge of changes in aerosol and cloud amounts, which can be obtained from a wavelength not affected by ozone.

Fioletov et al. (2001) have made ground-based estimates of erythemal irradiance changes from two Brewer spectrometer stations (Montreal and Edmonton), and found that the UV-B trends were similar to those expected from changes in ozone alone, but with much larger uncertainty because of clouds and aerosols.

5.4 UV in the Polar Regions

The expansion of the Antarctic polar vortex during the 1990s, both in spatial and temporal extent into early summer, has increased the frequency of elevated UV-B episodes over sub-Antarctic populated areas (Rousseaux et al., 1999). These episodes are no longer just small pockets of ozone depleted stratospheric air coming from the break-up of the polar vortex, but include occasional excursions of the polar vortex edge over Ushuaia, Argentina and Punta Arenas, Chile. This occurred 44 times in the years 1997, 1998, and 2000 combined, with some episodes lasting three to four days. Surface measurements show average erythemal UV increases of about 70% over Ushuaia (54.47°S) since 1997, and episodic total UV-B increases of up to 80% over Punta Arenas (53.08°S) (WMO, 2007).

Diaz et al. (2003) show that Barrow, Alaska, has experienced UV-B increases related to springtime ozone depletion in March and April, but these increases are a factor of ten smaller than those observed at the southern high latitudes. Summertime low-ozone episodes in the Arctic also affect surface UV-B irradiances. These summertime events result from gas-phase chemistry involving nitrogen and hydrogen cycles, which become very efficient during the 24-hour insolation that occurs in the Arctic summer. During summer 2000, two low- ozone episodes brought about erythemal UV increases in order of 10%−15%, each lasting more than five days (WMO, 2007).

The measured amounts of UV irradiance at Palmer Station, Antarctica (64°S) and San Diego, CA (32°N), show that for all seasons, other than spring in Antarctica, there is a decrease in UV-B irradiance caused by the increased path through the atmosphere resulting in less UV-B than observed in San Diego (Fahey, 2007). The Antarctic ozone depletion that occurs each spring causes the UV-B portion of the erythemally-weighted irradiance to increase dramatically to where it exceeds even the summertime values observed in San Diego. Similar wide-area springtime low ozone amounts do not occur in the Arctic region because of the degree of meteorological wave activity in the north that leads to a weaker polar vortex and higher ozone amounts. Southern Hemisphere ozone depletion events have extended further north over Southern Africa, parts of Australia, and New Zealand.

5.5 Human Exposure to UV

From the viewpoint of human exposure to UV, the maximum clear-sky UV irradiance and exposure occurs in the equatorial zone latitudes, ±23.3°, following the seasonal sub-solar point, and at high mountain altitudes. In general, UV erythemal, UV-A, and UV-B irradiance decreases with increasing latitude outside of the equatorial zone, due to the decreases in maximum daily noon solar elevation angles and for UV-B increases in ozone amount. An exception occurs for UV-B wavelengths at southern mid- to high-latitudes when reduced ozone amounts from the Antarctic ozone hole remain late into the spring and are pushed away from Antarctica toward the lower latitudes. For example, UV measurements indicate that the equatorial UV-B irradiance levels can occur in the southern part of South America for several days.

Global images of daily-integrated UV erythemal exposure (kJ per m^2), averaged during the months of January (Southern Hemisphere summer), July (Northern Hemisphere summer), and the two equinox months of September and March, are shown in Fig. 5.14 (based on WMO, 1999). Because of cloud cover, the high equatorial clear-sky irradiances do not translate into the highest monthly cumulative exposures. The maximum erythemal doses near the equator occur when the sun is directly overhead during March, which has lower cloud cover than during September. The difference is related to the annual cycle of the cloud cover associated with

the Intertropical Convergence Zone (ITCZ), which is usually over the equator in September, but is south of the equator in March. Two examples of very high UV exposures occur in the South American Andes (e.g., the sparsely populated Atacama Desert in Chile at 4,400 m to 5,600 m altitude, and in the city Cuzco, Peru) during January and in the Himalayan Mountains (over 100 peaks exceeding 7,000 meters) during July, as shown in Fig. 5.14. In both Southern Hemisphere cases, the sun is nearly overhead in January when the earth is also closest to the sun. Excluding high altitude locations, the largest monthly UV exposures occur in Australia and South Africa during summer (January) because of the very low amount of day-to-day cloud cover from late spring to early autumn. Other mid-latitude, low altitude relatively cloud-free areas also receive high doses, e.g., summertime (July) in the southwest U.S. and the Mediterranean countries.

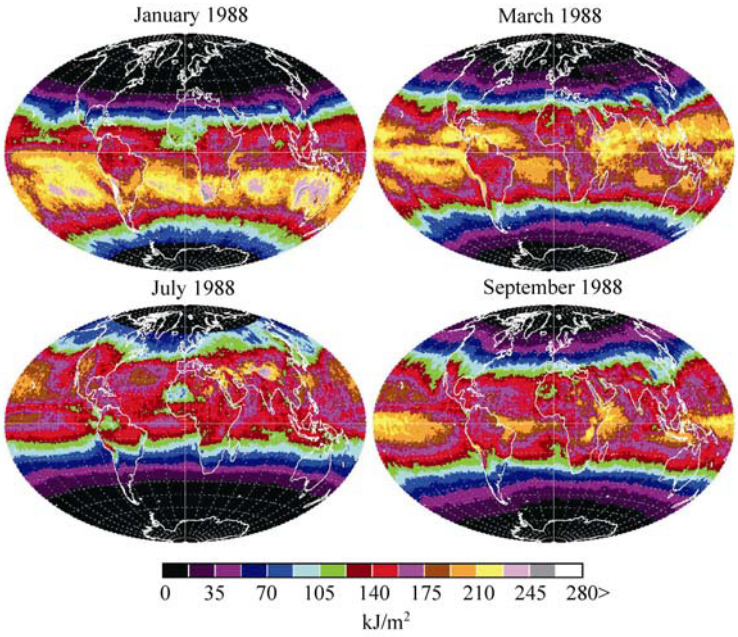

Figure 5.14 Erythemal exposure kJ per m^2 for the months of January, March, July, and September 1988 (from WMO, 1999) based on Nimbus-7/TOMS ozone and reflectivity data. These extreme levels are not seen in the September 1988 panel because the sun is just beginning to rise over Antarctica and the 1988 ozone depletion was not extreme

Other factors contribute to the high Southern Hemisphere UV doses. There is a five million km decrease (3%) in Earth-Sun distance (perihelion near January 3) during the Southern Hemisphere summer, as compared to the Northern Hemisphere summer (aphelion near July 4), causing a 6% increase in summer irradiance in the Southern Hemisphere for a couple of weeks around perihelion. Average

summer ozone in the Southern Hemisphere (270 DU) is lower than the Northern Hemisphere (320 DU) by about 13% which would lead to a 13% increase in 310 nm and a 26% increase in 305 nm irradiance. The exact percentage of increase is a function of latitude. In general, the Southern Hemisphere has fewer pollution aerosols, which can cause a small increase in UV irradiance relative to the Northern Hemisphere.

After latitude, the biggest factor affecting mid- and low-latitude exposure to UV radiation is the amount of cloud cover during the summer months. Satellite measurements of reflectivity indicate that there are some regions where there are long-term reflectivity increases (more cloud cover) over land in a few places, such as over the Indian Ocean, parts of Morocco and Algeria, northern Mexico/ southern U.S., and Canada. However, there are decreases in cloud cover over central U.S., northern Europe (60°N, 20°E), Kazakhstan (80°E 45°N), Argentina-Chile, and also smaller decreases over Australia and New Zealand that produce corresponding increases in time-integrated solar irradiance (exposure) reaching the ground (Herman et al., 2009b). While the decreasing cloud reflectivity increases solar radiation reaching the ground, changes in ozone are important for UV-B since it affects the clear-sky days when the irradiance is at a maximum for that day and latitude.

In Australia and other countries, any increase in UV exposure is especially detrimental to the European portion of the population that has minimal natural UV protection for skin cancer (Diffey, 1991; and a more general reference for health impact, Lucas et al., 2006), eye cataracts (Taylor, 1991), suppression of the immune system (Vermeer et al., 1991), and to ecosystem biology (Ghetti et al., 2006). Based on U.S. National Institute of Health (NIH) data (Devesa et al., 1999), similar skin cancer problems are present in the U.S., with more skin cancer occurring at lower latitudes where the UV exposure is higher. The seriousness of the very high UV exposure problem is observed in Australia where skin cancer rates have increased dramatically (20% for basal cell, to 788 per 100,000, and over 90% for squamous cell, to 321 per 100,000 carcinomas) based on household surveys in 1985, 1990, and 1995 (Staples et al., 1998). This compares to the U.S. National Cancer Institute's estimate (Devesa et al., 1999) of 14.5 per 100,000 for the U.S. Skin cancer incidence by skin type has been estimated by the U.S. National Cancer Institute's Surveillance, Epidemiology, and End Results (SEER) Program, which states that Caucasian people have the highest melanoma incidence, followed by a much lower rate for Hispanics, African Americans, and with the lowest incidence for Asian Pacific islanders.

The effects of custom or culture can be seen in Europe with large populations of light-skinned people living at fairly high latitudes (e.g., Stockholm, Sweden at 59.3°N, London, England at 51.5°N). However, there is a major difference in non-melanoma cancer incidence rates between citizens of Sweden (15 per 100,000) and the citizens of the United Kingdom (5 per 100,000) based on data from 1995 (Qiu and Marugame, 2008).

At higher latitudes in the Northern Hemisphere, where there is much more cloud cover than in Australia (e.g., central Europe 50°N, northern U.S., and Canada), a small decrease in cloud cover and ozone may produce the beneficial effect of increasing natural vitamin D production from increased UV-B exposure during the spring and summer months (Grant, 2002; McKenzie et al., 2003; Holick, 2004) without producing greatly enhanced rates of skin cancer. In the U.S., NIH data shows (Devesa et al., 1999) that increased solar exposure appears to correlate by latitude with decreases in some internal cancers along with increases in skin cancer.

5.6 UV Index and Units

Erythemal irradiance is frequently expressed in terms of the UV index = 25 mW per m^2 = 2.5 μW per cm^2. The index is an arbitrary unit such that very high values reported by weather services have a UV index of 10 (25 μW per cm^2). Erythemal exposure or dose is a time-integrated quantity normally expressed in kJ per m^2. Many high altitude locations with extreme UV amounts can exceed 10 on clear days. The weather service for the populated region near Cuzco, Peru, frequently reports a UV index of 10 to 11 for extended periods and occasionally has a UV index that reaches 25, the latter based on TOMS ozone data analysis (Liley and McKenzie, 2006). Spectral irradiance is expressed in mW per m^2 per nm. The solar irradiance has a peak value of about 2,100 mW m^{-2} nm^{-1} at about 450 nm. Sky radiance is expressed in mW m^{-2} nm^{-1} per steradian. Zenith sky irradiance for 0.5° FOV is of the order of 10^{-5} of the solar irradiance in the vicinity of 400 nm, but the ratio increases with decreasing wavelength because of increasing Rayleigh scattering in the UV wavelengths.

5.7 Action Spectra and Irradiance Trends

An action spectrum $A(\lambda)$ is a weighting function of wavelength λ that estimates the relative strength of a process (e.g., biological process or material degradation) for each wavelength in a range from λ_1 to λ_2. The action spectrum is multiplied by the irradiance $I(\lambda,t)$ to obtain a production function $P_{\mathrm{ACT}}(t)$. A direct comparison of dose amounts for any causal effect is not given by $A(\lambda)$, but just indicates the relative effect of each wavelength. Frequently, what is wanted is the time integrated effect of the process E_{F} over a specified time interval t_1 to t_2. The quantities P_{ACT} and E_{F} can be used to estimate the relative effect of exposure to solar radiation on different days at some specified time, or cumulatively over some portion of a day or longer (Eqs. (5.15) and (5.16)).

$$P_{\mathrm{ACT}}(t) = \int_{\lambda_1}^{\lambda_2} I(\lambda,t)A(\lambda)\mathrm{d}\lambda \tag{5.15}$$

$$E_{\mathrm{F}} = \int_{t_1}^{t_2} P(t)\mathrm{d}t \tag{5.16}$$

Typical action spectra have been estimated for skin reddening for Caucasian males, plant damage, vitamin D production, non-melanoma cancer production, and DNA damage, etc. The vitamin D action spectrum $A_{\text{Vit-D}}$ is based on a digitization of the action spectrum graph presented by McLaughlin et al. 1988. The vitamin D production was obtained in the laboratory from "surgically separated skin." An accurate functional fit (Fig. 5.15(a)) to the published graph is given ($250\ \text{nm} < \lambda < 315\ \text{nm}$) in Table 5.2 along with functional fits to the graphs (Figs. 5.15(b), (c), (d)) for three other more common action spectra, A_{DNA} damage, plant growth A_{PLA}, and erythemal A_{ERY}.

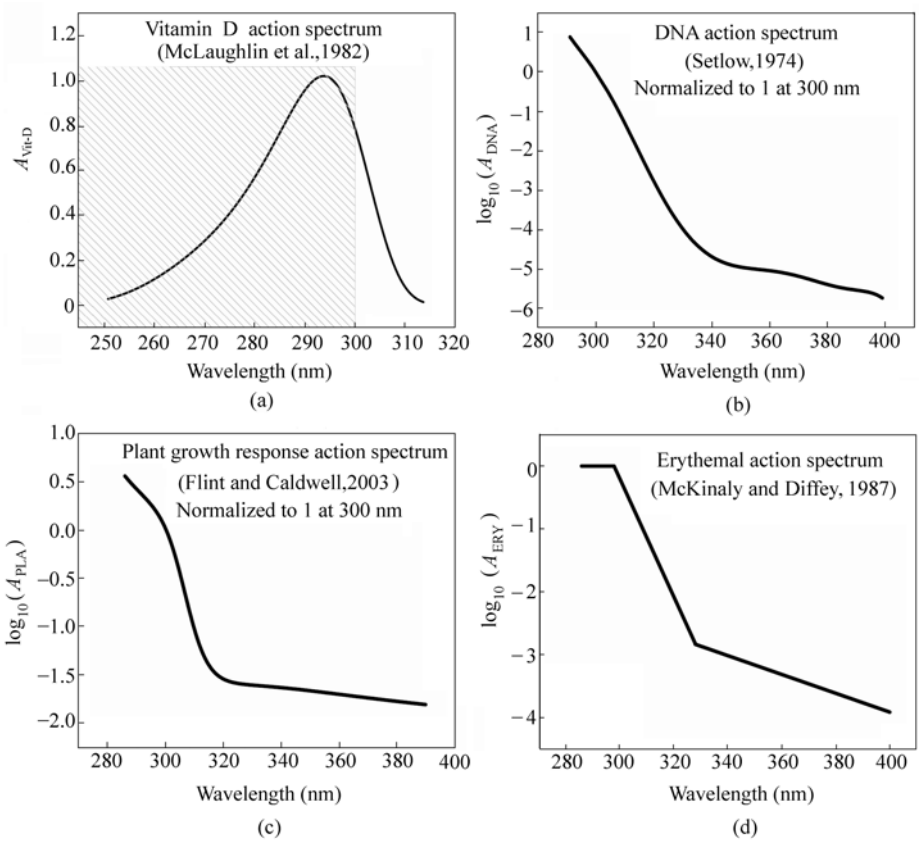

Figure 5.15 (a) Fit to vitamin D action spectrum (McLaughlin et al., 1982), $250\ \text{nm} < \lambda < 314\ \text{nm}$; (b) Fit to DNA damage action spectrum from (Setlow, 1974), $290\ \text{nm} < \lambda < 400\ \text{nm}$; (c) Fit to plant growth response action spectrum (Flint and Caldwell, 2003), $285\ \text{nm} < \lambda < 390\ \text{nm}$; (d) Fit to erythemal action spectrum (McKinlay and Diffey, 1987), $250\ \text{nm} < \lambda < 400\ \text{nm}$

Figures 5.16 and 5.17 show the result of multiplying respective action spectra by the solar flux (Fig. 5.2) at the ground for an atmosphere with 300 DU of ozone and SZA = 0° (typical or the equatorial band with overhead sun). From a practical perspective, wavelengths below 300 nm have little effect at sites near sea level, because there are too few photons that are able to penetrate the atmosphere. Altitude must be taken into account at higher altitude sites, even though most of the short wavelength photons are absorbed by stratospheric ozone, but the numbers that do penetrate the stratosphere are not reduced as much by Rayleigh multiple scattering compared to the boundary layer atmosphere. The effect for DNA damage and vitamin D production decreases rapidly for longer wavelengths, especially for larger SZA typical of mid-latitudes. The erythemal effect persists into the UV-A

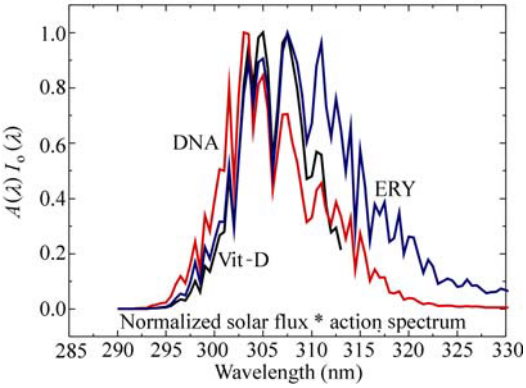

Figure 5.16 Action spectra (DNA, vitamin D, and ERY) multiplied by the solar flux at the ground for 300 DU of ozone and SZA = 0°

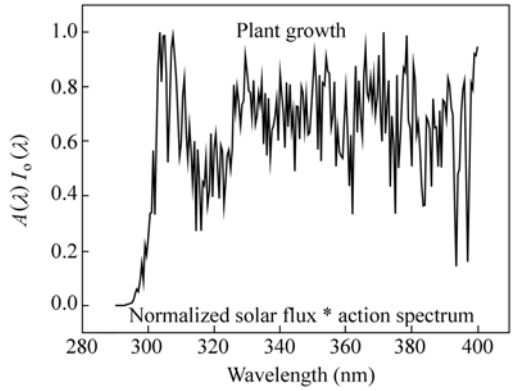

Figure 5.17 Action spectrum (plant growth) multiplied by the solar flux at the ground for 300 DU of ozone and SZA = 0°

range, which is why it is important for sunscreen preparations to protect to as long a wavelength as is possible. Finally, the plant growth spectrum (Fig. 5.15(c)) spans both UV-B and UV-A, and extends into the VIS wavelengths.

The accuracy of action spectra are usually not specified since they are meant to convey the response that occurred during a particular set of experiments that are highly specific to the particular samples that were examined. This is particularly true for the three spectra that pertain to human response to UV light. None of these spectra apply to any specific individual or group of people, but are just indicative of a process. The spectra can be used to give an idea of how a process would change if there were a change in the UV irradiance for a sample that had an approximate average response that was similar to the above spectra. The best-known example of this is the use of the UV index based on the erythemal action spectrum. Here the accuracy of the UV index is limited to no better than 10% (i.e., an integer scale from 0 to 10), but nonetheless, the index is useful for estimating when conditions are likely to cause harm from exposure to UV irradiance. All of the action spectra should be considered in a similar manner.

As discussed in Section 5.3.1, the behavior with respect to ozone change of action spectrum weighted summed irradiances is not the same as for monochromatic irradiances. The fractional change is approximated by a power law in RAF described in Section 5.3.2, which has been demonstrated to hold for a wide range of ozone values Ω with constant RAF for each SZA. Rearranging Eq. (5.3) in terms of fractional differences,

$$(F_1 - F_2)/F_2 = [1 + (\Omega_1 - \Omega_2)/\Omega_2]^{-\mathrm{RAF}(\theta)} - 1 \qquad (5.17)$$

However, the RAF(θ), where θ = SZA, must be empirically derived for each action spectrum and each SZA. This has been done for the erythemal irradiance F_{ERY} using measurements from Mauna Loa, Hawaii (Bodhaine et al., 1997). The resulting variation of RAF(θ) with SZA is shown in Fig. 5.18, along with a theoretical calculation based on Eq. (5.4) applied to each wavelength and summed with erythemal weighting. This shows that the empirical power law behavior $F_1/F_2 = (\Omega_2/\Omega_1)^{\mathrm{RAF}(\theta)}$ can be explained by application of the physically based Beer's Law for absorption in the atmosphere. The behavior with SZA is as expected from a mix of UV-B and UV-A wavelengths, as the importance of UV-B decreases with increasing SZA. In addition to standard action spectra, a recent WMO report (Seckmeyer et al., 2005) has developed an RAF(θ,Ω) analysis for the specific response of particular types of broadband instruments that are intended to approximate the erythemal response function. They also present an analysis of RAF(θ,Ω) for the exact erythemal weighting function A_{ERY} (Table 5.4) for the ozone range from 100 DU to 600 DU. In all of the work discussed here RAF(θ,Ω) = RAF(θ) by limiting the range of Ω to 200 DU < Ω < 600 (see Appendix 5.1).

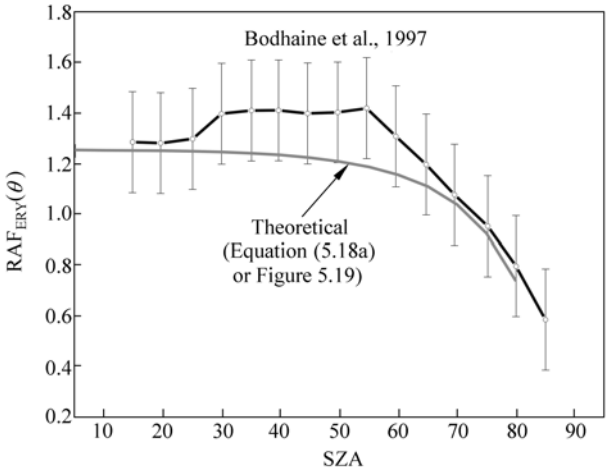

Figure 5.18 $\mathrm{RAF_{ERY}}(\theta)$ variation with $0 < \theta < 85^\circ$ for the erythemal action spectrum from data obtained at Muana Loa, Hawaii (Bodhaine et al., 1997) compared with a theoretical calculation based on summation over wavelengths using A_{ERY} and Eq. (5.4) yielding the form of Eq. (5.17), which is fitted by Eq. (5.18a) for erythemal irradiance (Herman, 2009)

Table 5.4 Function fit to four UV action spectra of Fig. 5.8

Fit to vitamin D spectrum (McLaughlin et al., 1988) $A_{\mathrm{Vit\text{-}D}}$ $250\ \mathrm{nm} < \lambda < 314\ \mathrm{nm}$
$\log_{10}(A_{\mathrm{Vit\text{-}D}}) = (A + C\lambda^{0.5} + E\lambda + G\lambda^{1.5})/(1 + B\lambda^{0.5} + D\lambda + F\lambda^{1.5})$
$A = -0.9601647127133382$ $B = -0.1771944277419561$ $C = 0.1798847906875285$
$D = 0.01044079180885732$ $E = -0.01118449188229313$ $F = -0.00020464360877287360$
$G = 0.0002309087838152358$
Fit to DNA damage spectrum (Setlow, 1974) A_{DNA} $290\ \mathrm{nm} < \lambda < 400\ \mathrm{nm}$
$\log_{10}(A_{\mathrm{DNA}}) = (A + C\lambda^{0.5} + E\lambda)/(1 + B\lambda^{0.5} + D\lambda + F\lambda^{1.5})$
$A = -0.1090717334891702$ $B = -0.1578036701734071$ $C = 0.01546956801974633$
$D = 0.008268275171175154$ $E = -0.000529417616572146$ $F = -0.0001436582640327567$
Fit to plant growth response action spectrum (Flint and Caldwell, 2003) A_{PLA}
$\log_{10}(A_{\mathrm{PLA}}) = (A + C\lambda^{0.5} + E\lambda)/(1 + B\lambda^{0.5} + D\lambda + F\lambda^{1.5})$ $285\ \mathrm{nm} < \lambda < 390\ \mathrm{nm}$
$A = -2.747265993518105$ $B = -0.1791860260727771$ $C = 0.4772684658484249$
$D = 0.01068302156756403$ $E = -0.02764643975624155$ $F = -0.0002119599411078172$
$G = 0.0005339842703179307$
Fit to erythemal action spectrum (McKinlay and Diffey. 1987) A_{ERY}
$\log_{10}(A_{\mathrm{ERY}})$ $250\ \mathrm{nm} < \lambda < 400\ \mathrm{nm}$
$\log_{10}(A_{\mathrm{ERY}}) = 0$ $250\ \mathrm{nm} < \lambda < 298\ \mathrm{nm}$
$\log_{10}(A_{\mathrm{ERY}}) = 0.094(298 - \lambda)$ $298\ \mathrm{nm} < \lambda < 328\ \mathrm{nm}$
$\log_{10}(A_{\mathrm{ERY}}) = 0.015(139 - \lambda)$ $328\ \mathrm{nm} < \lambda < 400\ \mathrm{nm}$

Theoretically calculated $\mathrm{RAF}(\theta)$ values for all four action spectra in Fig. 5.15 are given in Fig. 5.19, and the fitting functions for each RAF in Table 5.5,

Eqs. (15.8a~15.8d), for the ozone range from 200 DU to 600 DU, which gives an RAF(θ) that is independent of the ozone value. If the range is extended to 100 DU, the RAF(θ,Ω) depends on the ozone amount and SZA. The behavior of some action spectra RAFs with SZA (e.g., DNA) is similar to single wavelength RAFs for relatively narrow action spectra mostly contained in the UV-B region; namely, increasing RAF with SZA. More broadly-based spectra have RAF values that are nearly constant for SZA < 40°, and decrease for larger values of SZA. Very wide spectra, such as the Plant Growth spectrum, decrease for all SZA > 0.

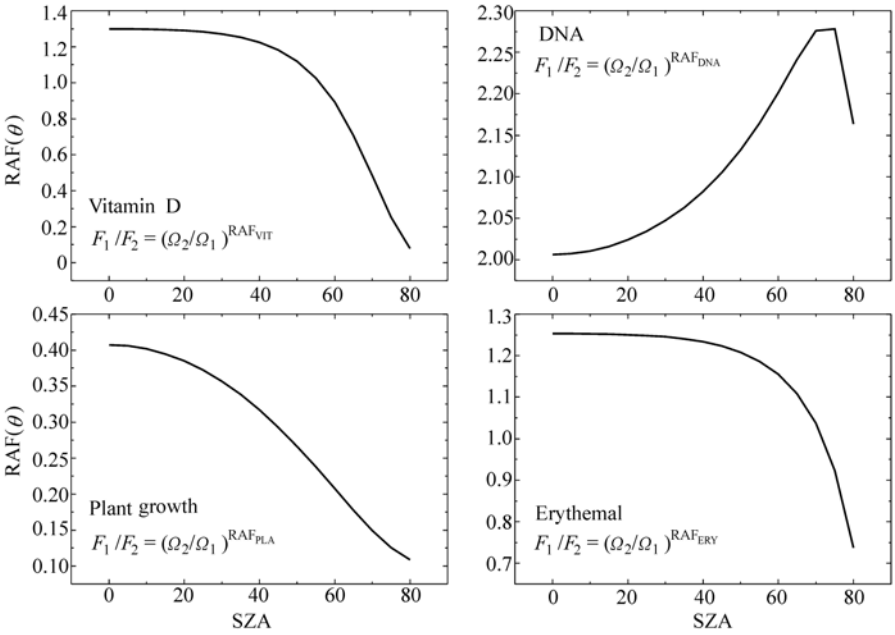

Figure 5.19 The variation of RAF with SZA for the four spectra in Fig. 5.15. Note that RAF_{ERY} and RAF_{VIT} look similar because of different scales (200 DU < Ω < 600 DU)

The reason that scattering can be neglected when calculating change in irradiance is that the scattered radiance is linearly proportional to the direct solar beam when stratospheric ozone is the primary absorber. The calculation may not be accurate for strongly absorbed wavelengths at large SZA when the direct solar beam is very small compared to the scattered irradiance. When this happens, the path through the atmosphere to the ground is the expected slant path through the stratosphere, which changes to a nearly vertical path for scattered irradiance that occurs lower in the atmosphere (Umkehr effect). This shortens the optical path and reduces the sensitivity to ozone change that occurs in the troposphere. If ozone changes in the stratosphere are much larger than in the troposphere, $F_1/F_2 = (\Omega_2/\Omega_1)^{RAF(\theta)}$ is still a good approximation, since scattering can be neglected for estimations of irradiance change.

Table 5.5 Fitting functions for the action spectra RAF of Fig. 5.19

$$\mathrm{RAF}_{\mathrm{ERY}} = (A + C\theta^{0.5} + E\theta)/(1 + B\theta^{0.5} + D\theta + F\theta^{1.5}) \quad (5.18a)$$

$A = 1.253034387380404$ $B = -0.1893942742785442$
$C = -0.2374988749526192$ $D = 0.008753703248421607$
$E = 0.01109085001133105$ $F = 2.163425112458424\mathrm{D}{-05}$

$$\mathrm{RAF}_{\mathrm{DNA}} = (A + C\theta^{2} + E\theta^{4})/(1 + B\theta^{2} + D\theta^{4}) \quad (5.18b)$$

$A = 2.006603342348651$ $B = -0.000222243468041799$
$C = -0.0004040537916876323$ $D = 1.23788082612675\mathrm{D}{-08}$
$E = 1.861486615239331\mathrm{D}{-08}$

$$\mathrm{RAF}_{\mathrm{VIT}} = (A + C\theta^{0.5} + E\theta + G\theta^{1.5})/(1 + B\theta^{0.5} + D\theta + F\theta^{1.5}) \quad (5.18c)$$

$A = 1.300000361376985$ $B = -0.2561979971919163$
$C = -0.3331173671966876$ $D = 0.02040664839011024$
$E = 0.02657302492632673$ $F = -0.0004560385514125725$
$G = -0.0006221828632328866$

$$\mathrm{RAF}_{\mathrm{PLA}} = (A + C\theta^{0.5} + E\theta)/(1 + B\theta^{0.5} + D\theta) \quad (5.18d)$$

$A = 0.4073412230744607$ $B = -0.1992738307220675$
$C = -0.08017040437930313$ $D = 0.01140308620531996$
$E = 0.004045533964044966$

The percent change in zonal average clear-sky erythemal irradiance as a function of latitude can be estimated from the 30-year monthly and zonal averaged ozone time series by using Eqs. (5.17) and (5.18a) (Fig. 5.20). The estimations are restricted to latitudes between 53°S to 53°N because the estimation of the RAF was for SZA < 80°. During the winter solstice, at 53° latitude, the noon SZA is 76°. The estimation of RAFs for large SZA > 80° could be done with a spherical geometry corrected radiative transfer analysis.

The results in Fig. 5.20 show that there have been large changes in potentially damaging UV-B radiation at all wavelengths. The monochromatic changes were estimated from Eq. (5.4) because some of the ozone changes were sufficiently large as to result in a small error using the differential form in Eq. (5.1). The high latitude values may have a very small error caused by neglecting the spherical geometry correction to sec(SZA) for winter conditions at 52.5° latitude when the noon SZA reached 75.8°. The effect would be to slightly reduce the optical path and the estimated change in irradiance. At lower latitudes, the effect is negligible.

Since the DNA damage RAF, which is dominated by the behavior between 300 nm and 310 nm (Fig. 5.16), is similar in shape with respect to SZA to the monochromatic RAF, the percent increase will be much larger for DNA damage than for the erythemal spectrum. Figures 5.21 and 5.22 present the monthly percent change of 100 $\mathrm{d}F_{12}/F_2$ in 305 nm irradiance and the DNA damage weighted irradiance $P_{\mathrm{DNA}}(\mathrm{Month}, \theta)$ from 1979 to 2008. As expected, the change in percent is similar for low latitudes where the ozone change is fairly small. For larger Ω

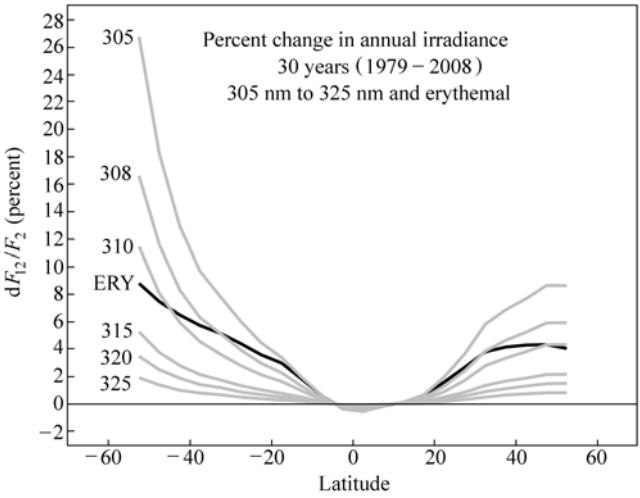

Figure 5.20 The percent change in annual clear-sky erythemal irradiance (ERY solid black) for 30 years during the period 1979 to 2008, based on Eqs. (5.17) and (5.18a), and the monthly and zonal averaged ozone time series. The change in monochromatic 305, 308, 310, 315, 320, and 325 nm irradiance from Eq. (5.4) are also shown (gray)

changes at high southern latitudes, the behavior is somewhat different because of increased contribution to P_{DNA} (Eq. (5.15)) from wavelengths smaller than 305 nm for the summer months. The same summer effect is smaller at high northern latitudes because the ozone change is less (annual ozone change 3.5% compared to 7%, Fig. 5.22).

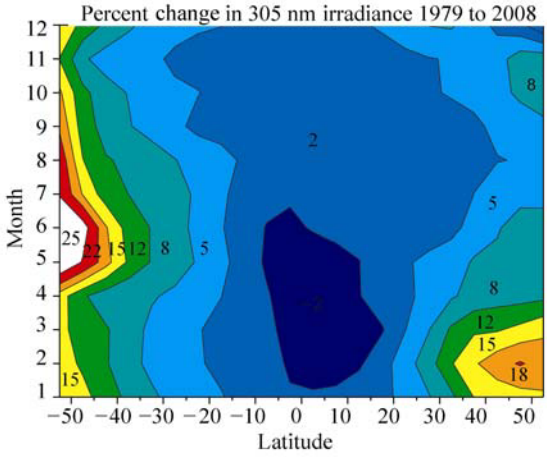

Figure 5.21 Percent change in clear-sky 305 nm irradiance from 1979 to 2008 as a function of month and latitude calculated from Eq. (5.4) and the monthly zonal average ozone data

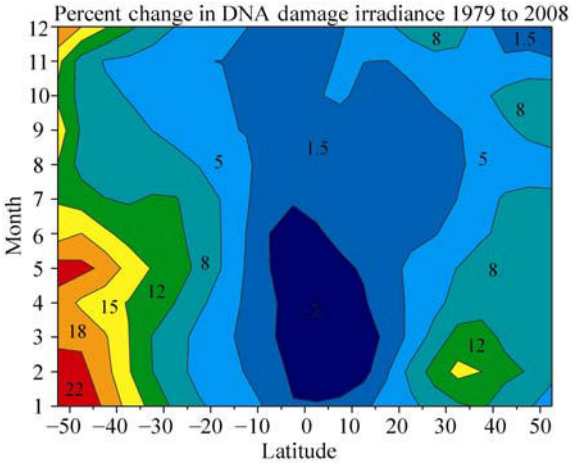

Figure 5.22 Percent change in clear-sky DNA damage spectrum weighted irradiance from 1979 to 2008 as a function of month and latitude calculated from Eq. (5.17), Table 5.2, and the monthly zonal average ozone data

From the viewpoint of population in the higher latitudes of the Northern Hemisphere, the increases in clear-sky P_{DNA} have been 5% − 8% during most of the spring and summer months when the solar UV irradiance exposure is at a maximum (more clear days as well as seasonally declining ozone going into the summer). The changes have been much larger in the higher latitudes of the Southern Hemisphere during the spring and summer months, ranging from 12% to over 20%, and extend to lower latitudes (a 12% to 15% increase between 30°S and 40°S and 18% to 22% between 40°S and 50°S). These are serious increases in damaging UV irradiance that likely would have been much worse in the absence of the chlorine limiting agreement contained in the Montreal Protocols and subsequent agreements.

5.8 UV Summary

Quantitative UV measurements have been made for the past 50 years with gradually growing sophistication in the instruments. Requirements for determining UV irradiance changes at the earth's surface are currently well understood and have been implemented at a number of sites. Measurements from ground-based instruments and estimations from satellite instruments around the globe show a mixture of UV-B increases and decreases that depend on changes in local cloud cover, and ozone and aerosol amounts.

Measurements of ozone and cloud plus aerosol reflectivity from satellites have been used to estimate the changes in UV-B for the past 30 years using data collected since 1979. The estimation of irradiance change can be obtained using radiative

transfer calculations, or from a simplified, yet accurate, approach using the "Radiation Amplification Factor." Based on the satellite ozone record, the summer average, clear-sky UV erythemal irradiance P_{ERY}, averaged over the 32.5°N latitude band, increased by about 8% from 1979 to the mid-1990s. Since the mid-1990s, P_{ERY} has decreased so that the current level is about 7% higher than it was at the start of the record in 1979. Similar, changes have occurred in the 32.5°S latitude band where the increase was about 7% in 2008 (Fig. 5.9). At higher latitudes, the annual average increase has been about 8% near the tip of South America (50°S), and about 4.5% at 50°N (Fig. 5.20).

Because of increased sensitivity to ozone changes at 305 nm (near the peak of the DNA damage weighted irradiance P_{DNA}), the increases have been substantially larger. The change in annual average 305 nm at 32.5°S is about 8%, rising to about 23% at 50°S. In the Northern Hemisphere, the changes have been somewhat smaller, about 6% at 32.5°N and 8.5% at 50°N. These changes are large enough to cause concern for an increase in diseases related to sun exposure. The larger changes for 305 nm irradiance and P_{DNA}, which occurred at higher latitudes, were only partially moderated by a strongly latitude-dependent apparent increase in cloud and aerosol cover (preliminary estimate). When change in cloud cover is included, average annual increase in 305 nm irradiance at 50°S was about 17% over 30 years, while the increase at 50°N was about 11%. Clouds will have approximately the same effect on all UV wavelengths. Since, the change caused by just ozone was larger in the Southern Hemisphere than in the Northern Hemisphere, it implies that danger from human exposure on clear days has increased more in the Southern Hemisphere than in the Northern Hemisphere. The increases for DNA damage irradiance P_{DNA} have been substantially larger than for P_{ERY}, since the weighting is more towards the shorter wavelengths. The effect is much larger in the Southern Hemisphere during spring and summer than in the Northern Hemisphere at higher latitudes, 30° to 50° (Fig. 5.22).

Ground-based measurements of surface UV trends present a challenge that can be overcome with proper filtering of the data for cloud-free conditions along with simultaneous aerosol measurements. Ultraviolet estimates from satellite measurements of ozone, aerosols, and cloud reflectivity are averages over large areas on the order of 25 km to 100 km, which minimizes many problems with local variability of cloud and aerosol amounts. Both ground and satellite UV estimates are critically dependent on establishing and maintaining an accurate calibration over the lifetime of an instrument and between successive instruments. Ground-based measurements are essential to provide validation of satellite calibration and as a bridge between successive satellite instruments.

While the Northern Hemisphere UV irradiance maximum in 1993 was associated with the massive equatorial Mt. Pinatubo eruption in 1991 (Kerr and McElroy, 1993, Bhartia et al., 1993), a portion of the total increase occurred before 1991 and was associated with ozone destruction from chlorine loading in the atmosphere

before being limited by the Montreal Protocol. Though there have been significant zonal average ozone decreases over 30 years at most latitudes (except the equator), even larger chlorine-driven ozone decreases and UV-B increases were prevented by this and subsequent agreements that were effective for limiting releases of chloroflourocarbons (CFCs) and other chlorine bearing compounds, with CFCs being almost completely phased out by 1995.

Because of the large observed changes in UV-B irradiance at mid- and high-latitudes, it is very important that we continue monitoring from both space and the ground. For space, it is essential that we have continuous well-calibrated data sets from successive near-noon, sun-synchronous satellites, with at least a one-year overlap. The calibration of satellite instruments is an extended effort that must be performed over the life of the satellite using in-flight data leading to occasional reprocessing (perhaps once every two years) of the entire dataset. Comparisons with ground-based UV irradiance and radiance data play an essential role in traditional validation and identification of problems with either satellite or ground-based instruments. For this purpose, a few well-characterized and maintained spectrometers are preferable to large networks of lesser instruments. The few instruments should be located in both clean and moderately polluted sites, and in key locations (e.g., mountains) where satellite estimations may be intrinsically in error. More effort should be put into instruments and procedures that characterize the atmosphere in terms of absorption, scattering, and composition rather than just measuring irradiance.

Appendix 5.1 Calculating RAF(θ)

If the RAF is calculated directly from the power law definition $F_1/F_2 = (\Omega_2/\Omega_1)^{\mathrm{RAF}}$ or $\mathrm{RAF} = \ln(F_1/F_2)/\ln(\Omega_2/\Omega_1)$, the result will have a dependence on ozone amount for any range of Ω_1 relative to the reference amount Ω_2 (Fig. 5.A1).

In this study, the RAF is calculated as the best fit to the function $U(\Omega_2/\Omega_1)^{\mathrm{RAF}}$ with the requirement that U is approximately 1 (Fig. 5.A2). This approximation works well for the entire range of SZA (Fig. 5.A3), the ozone range 200 DU to 600 DU, and for all four action spectra discussed in this study. The result is a small error in the estimation of action spectra irradiance change, if the ozone independent RAF is used in the power law formula. If more accuracy is needed for the erythemal spectrum, the parameter $U(\theta)$ is given by $U_{\mathrm{ERY}} = (A + C\theta^{0.5} + E\theta)/(1 + B\theta^{0.5} + D\theta + F\theta^{1.5})$ with the coefficients given in Table 5.A1. $0.95 < U_{\mathrm{ERY}}(\theta) < 0.99$. Similar functions can be derived for other action spectra.

If the range is extended to $100\ \mathrm{DU} < W < 600\ \mathrm{DU}$, then the functional form changes (Fig. 5.A4) for $\mathrm{SZA} < 50^\circ$ and the form $U(\Omega_2/\Omega_1)^{\mathrm{RAF}}$ with an RAF value independent of Ω can no longer be used.

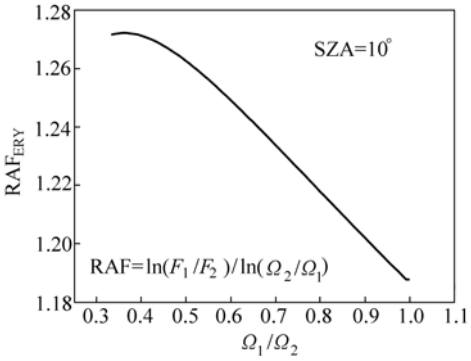

Figure 5.A1 RAF computed from its definition, $\mathrm{RAF} = \ln(F_1/F_2)/\ln(\Omega_2/\Omega_1)$

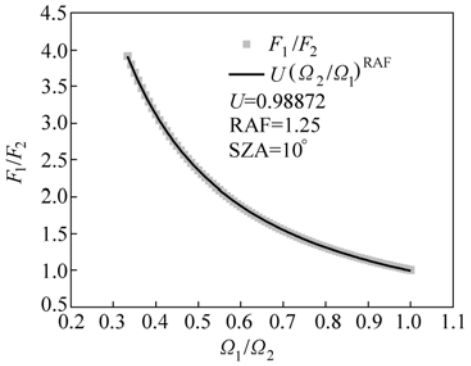

Figure 5.A2 RAF computed as best fit to irradiance ratios F_1/F_2 (gray squares) using $U(\Omega_2/\Omega_1)^{\mathrm{RAF}}$ (black line)

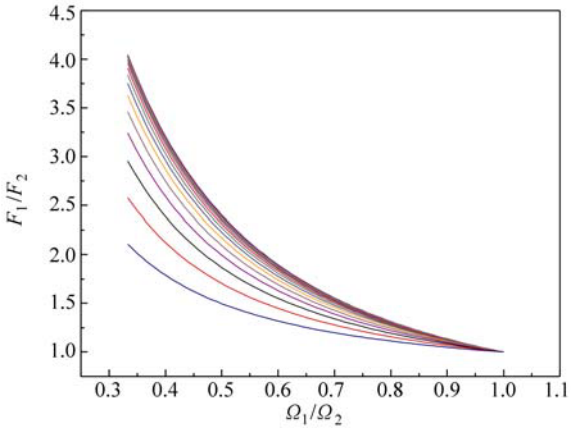

Figure 5.A3 F_1/F_2 for $0° < \mathrm{SZA} < 80°$ for 200 DU $< W <$ 600 DU

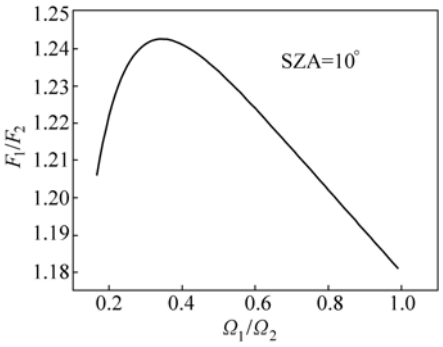

Figure 5.A4 Irradiance ratios when the ozone range is extended $100 < \Omega < 600$

Table 5.A1 $U_{ERY} = (A + C\theta^{0.5} + E\theta)/(1 + B\theta^{0.5} + D\theta + F\theta^{1.5})$

$A = 0.9893339422829114$	$B = -0.2091512249939112$
$C = -0.2065389508416529$	$D = 0.01116628089647472$
$E = 0.01084565669362034$	$F = -0.00001740267964926986$

Acknowledgements

This research was partly supported by the NASA MEASURES project for the reflectivity data. In addition, I would like to acknowledge the OMI, SBUV-2, and TOMS satellite analysis team for making the merged ozone time series available.

References

Bhartia PK, Herman JR, and Torres O (1993) Effect of Mt. Pinatubo aerosols on total ozone measurements from backscatter ultraviolet (BUV) experiments. J. Geophys. Res. 98: 18547 – 18554

Blumthaler M, Salzgeber M, and Ambach W (1995) Ozone and ultraviolet-B irradiances: experimental determination of the radiation amplification factor. Photochem Photobio 61: 159 – 162

Bodhaine BA, Dutton EG, Hofmann DJ, McKenzie RL, and Johnston PV (1997) UV measurements at Mauna Loa: July 1995 to July 1996. J. Geophys. Res. 102(D15): 19265 – 19273

Booth CR, Madronich S (1994) Radiation amplification factors: Improved formulation accounts for large increases in ultraviolet radiation associated with Antarctic ozone depletion. In: Weiler CS, Penhale PS (eds) Ultraviolet radiation in Antarctica: measurement and biological effects. Antarct Res Ser 62: 39 – 52

Brueckner C, Floyd LE, Lund PA, Prinz DK, and Vanhoosier ME (1994) In: Pap JM, Frolich C, Hudson HS, Solanki S (eds) The Sun as a Variable Star: Solar and Stellar Irradiance Variations. Cambridge Univ. Press, Cambridge, UK

Cede A, Herman J, Richter A, Krotkov N, and Burrows J (2006) Measurements of nitrogen dioxide total column amounts at Goddard Space Flight Center using a Brewer Spectrometer in direct sun mode. J. Geophys. Res. 111, D05304, DOI:10.1029/2005JD006585

Chubarova NY (2008) UV variability in Moscow according to long-term UV measurements and reconstruction model. Atmos. Chem. Phys. Discuss. 8: 893 – 906

Dave JV (1964) J. Opt. Soc. America, 54: 307

Devesa SS, Grauman DJ, Blot WJ, Pennello G, Hoover RN, and Fraumeni JF Jr. (1999) Atlas of cancer mortality in the United States, 1950 – 1994. Washington, DC: US Govt Print Off, NIH Publ. No. (NIH) 99 – 4564

Díaz S, Nelson D, Deferrari G, and Camilión C (2003) A model to extend spectral and multiwavelength UV irradiances time series: Model development and validation. J. Geophys. Res., 108(D4): 4150, doi:10.1029/2002JD002134

Diffey BL (1991) Solar ultraviolet radiation effects on biological systems. Review in Physics in Medicine and Biology 36(3): 299 – 328

Fahey DW (Lead Author) (2007) Twenty Questions and Answers About the Ozone Layer: 2006 Update, in Scientific Assessment of Ozone Depletion: 2006. Global Ozone Research and Monitoring Project Report No. 50, World Meteorological Organization, Geneva

Flint SD, and Caldwell MM (2003) A biological spectral weighting function for ozone depletion research with higher plants. Physiologia Plantarum 117: 137 – 144

Gao W, Slusser J, Gibson J, Scott G, and Bigelow D (2001) Direct-Sun column ozone retrieval by the ultraviolet multifilter rotating shadow-band radiometer and comparison with those from Brewer and Dobson spectrophotometers. J. Applied Optics 40: 3149 – 3156

Ghetti F, Bagnoli C, and Checcucci G (2006) Response to UV-B Radiation: Weighting Functions and Action Spectra, Environmental UV Radiation: Impact on Ecosystems and Human Health and Predictive Models Proceedings of the NATO Advanced Study Institute on Environmental UV Radiation: Impact on Ecosystems and Human Health and Predictive Models, Pisa, Italy, June 2001

Goering CD, L'Ecuyer TS, Stephens GL, Slusser JR, Scott G, Davis J, Barnard JC, and Madronich S (2005) Simultaneous retrievals of column ozone and aerosol optical properties from direct and diffuse solar irradiance measurements. J. Geophys. Res. 110, O5, D05204, 10.1029/2004JD005330

Hemminki K, Xu G, Kause L, Koulu LM, Zhao C, and Jansen CT (2002) Demonstration of UV-dimers in human skin DNA in situ 3 weeks after exposure. Carcinogenesis 23: 605 – 609

Herman JR, Hudson R, McPeters R, Stolarski R, Ahmad Z, Gu X-Y, Taylor S, and Wellemeyer C (1991) A new self-calibration method applied to TOMS/SBUV backscattered ultraviolet data to determine long term global ozone change. J. Geophys. Res. 96: 7531 – 7545

Herman JR, Newman PA, McPeters RD, Krueger AJ, Bhartia PK, Seftor CJ, Torres O, Jaross G, Cebula RP, Larko D, and Wellemeyer C (1995) Meteor-3/Total Ozone Mapping Spectrometer observations of the 1993 ozone hole. J. Geophys. Res. 100: 2973 – 2983

Herman JR, Bhartia PK, Ziemke J, Ahmad Z, and Larko D (1996) UV-B radiation increases (1979 – 1992) from decreases in total ozone. Geophys. Res. Lett. 23: 2117 – 2120

Herman JR, Krotkov N, Celarier E, Larko D, and Labow G (1999) Distribution of UV radiation at the Earth's surface from TOMS-measured UV-backscattered radiances. J. Geophys. Res. 104: 12059 – 12076

Herman JR, Larko D, and Ziemke J (2001a) Changes in the Earth's Global UV Reflectivity from Clouds and Aerosols. J. Geophys. Res. 106: 5353 – 5368

Herman JR, Celarier E, and Larko D (2001b) UV 380 nm reflectivity of the Earth's surface, clouds, and *aerosols*. J. Geophys. Res. 106: 5335 – 5351

Herman J, Cede A, Spinei E, Mount G, Tzortziou M, and Abuhassan N (2009a) NO_2 column amounts from ground-based PANDORA and MF-DOAS spectrometers using the Direct-Sun DOAS Technique: Intercomparisons and application to OMI validation. J. Geophys. Res. 114, D13307, doi: 10.1029/2009JD011848

Herman JR, Labow G, Hsu NC, and Larko D (2009b) Changes in cloud cover (1998 – 2006) derived from reflectivity time series using SeaWiFS, N7-TOMS, EP-TOMS, SBUV-2, and OMI radiance data. J. Geophys. Res. 114:D01201, DOI: 10.1029/2007JD009508

Herman JR (2009) Global Increase in UVB During the past 30 years 1979 to 2008. Accepted, J. Geophys. Res. 114: D01201, doi: 10.1029/2007JD009508

Holben BN, Eck TF, Slutsker I, Tanre D, Buis JP, Setzer A, Vermote E, Reagan JA, Kaufman Y, Nakajima T, Lavenu F, Jankowiak I, and Smirnov A (1998) AERONET — A federated instrument network and data archive for aerosol characterization. Rem. Sens. Environ. 66: 1 – 16

Holben BN, Tanre D, Smirnov A, Eck TF, Slutsker I, Abuhassan N, Newcomb WW, Schafer J, Chatenet B, Lavenue F, Kaufman YJ, Vande J Castle, Setzer A, Markham B, Clark C, Frouin R, Halthore R, Karnieli A, O'Neill NT, Pietras C, Pinker RT, Voss K, and Zibordi G (2001) An emerging ground-based aerosol climatology: Aerosol optical depth from AERONET. J. Geophys. Res. 106: 12067 – 12097

Holick MF (2004) Sunlight and vitamin D for bone health and prevention of autoimmune diseases, cancers, and cardiovascular disease. American Journal of Clinical Nutrition 80(6): 1678S – 1688S

Kalliskota S, Kaurola J, Taalas P, Herman JR, Celarier EA, and Krotkov NA (2000) Comparison of daily UV doses estimated from Nimbus-7/TOMS measurements and ground-based spectroradiometric data. J. Geophys. Res. 105: 5059 – 5067

Kerr JB, and McElroy CT (1993) Evidence for large upward trends of ultraviolet-B radiation linked to ozone depletion. Science 262: 1032 – 1034

Kerr JP, Thurtell GW, and Tanner CB (1967) An Integrating Pyranometer for Climatological Observer Stations and Mesoscale Networks. Journal of Applied Meteorology 6: 688 – 694

Krotkov NA, Bhartia PK, Herman JR, Fioletov V, and Kerr J (1998) Satellite estimation of spectral surface UV irradiance in the presence of tropospheric aerosols 1: Cloud free case. J. Geophys. Res. 103: 8779 – 8793

Krotkov NA, Herman JR, Bhartia PK, Ahmad Z, and Fioletov V (2001) Satellite estimation of spectral surface UV irradiance 2: Effect of horizontally homogeneous clouds. J. Geophys. Res. 106: 11743 – 11759

Krotkov N, Bhartia PK, Herman J, Slusser J, Scott G, Labow G, Vasilkov AP, Eck TF, Dubovik O, and Holben BN (2005) Aerosol ultraviolet absorption experiment (2002 to

2004), Part 2: Absorption optical thickness, refractive index, and single scattering albedo. Opt. Eng. 44(4) 041005: 1 – 17

Liley, BJ, and McKenzie RL (2006) Where on Earth has the highest UV? UV Radiation and its Effects: An Update. NIWA Science, Hamilton, NZ

Lin B, Stackhouse Jr PW, Minnis P, Wielicki BA, Hu Y, Sun W, Fan T-F, and Hinkelman LM (2008) Assessment of global annual atmospheric energy balance from satellite observations. J. Geophys. Res. 113, D16114, doi:10.1029/2008JD009869

Lucas R, McMichael T, Smith W, and Armstrong B (2006) Solar ultraviolet radiation: Global burden of disease from solar ultraviolet radiation. Environmental Burden of Disease Series, No. 13, WHO Report

Madronich S (1993) The atmosphere and UV-B radiation at ground level. In: Björn LO, Young AR (eds) Environmental UV Photobiology. Plenum Press, New York, pp. 1 – 39

McClintock W, Rottman GJ, and Woods T (2000) Solar Stellar Irradiance Experiment Ⅱ (SOLSTICE Ⅱ) for the NASA Earth Observing System's Solar Radiation and Climate Experiment mission. SPIE 4135: 225 – 234

McKenzie RL, Bjorn LO, Bais A, and Hyasd M (2003) Changes in biologically active ultraviolet radiation reaching the earth's surface. Photochemical Photobiological Sciences 2: 5 – 15

McKinlay AF, and Diffey BL (1987) A reference action spectrum for ultraviolet induced erythema in human skin. In: Passchier WR, Bosnjakovic BFM (eds.) (1987) Human Exposure to Ultraviolet Radiation:Risks and Regulations. Elsevier, Amsterdam

Qiu D, and Marugame T (2008) Comparison of time trends in skin cancer incidence (1973 – 1997) in East Asia, Europe and USA, from cancer incidence in five continents. Japan J. of Clinical Oncology 38: 234 – 236

Roderick ML, and Farquhar GD (2002) The cause of decreased pan evaporation over the past 50 years. Science 298: 1410 – 1411

Rousseaux MC, Ballaré CL, Giordano CV, Scope AL, Zima AM, Szwarcberg-Bracchitta M, Searles PS, Caldwell MM, and Díaz SB (1999) Ozone depletion and UV-B radiation: Impact on plant DNA damage in southern South America. Proceedings of the National Academy of Sciences USA 96(26): 15310 – 15315

Rozema J, Van Geel B, Björn LO, Lean J, and Madronich S (2002) Toward solving the UV puzzle. Science 296 31: 1621 – 1622

Seckmeyer G, Bias A, Bernhard G, Blumthaler M, Booth CR, Lantz K, Mckenzie RL, Disterhoft P, and Webb A (2005) Instruments to measure Solar Ultraviolet radiation, Part 2: Broadband Instruments Measuring Erythemally Weighted Solar Irradiance. World Meteorological Organization Report 164, WMO TD-No.1289

Setlow RB (1974) The wavelengths in sunlight effective in producing cancer: a theoretical analysis. Proceedings of the National Academy of Sciences USA 71: 3363 – 3366

Slusser J, Gibson J, Bigelow D, Kolinski D, Disterhoft P, Lantz K, and Beaubien A (2000) Langley method of calibrating UV filter radiometers. Journal of Geophysical Research 105: 4841 – 4849

Staehelin J, Renaud A, Bader J, McPeters R, Viatte P, Hoegger B, Bugnion V, Giroud M, and Schill H (1998) Total ozone series at Arosa (Switzerland): Homogenization and data comparison. Journal of Geophysical Research 103(D5): 5827 – 5841

Staehelin J, and Weiss AK (2001) Swiss history of atmospheric ozone research and results of long-term Swiss ozone measurements. Ozone: Science and Engineering 23: 461 – 466

Stanhill G, and Cohen S (2001) Global dimming: A review of the evidence for a widespread and significant reduction in global radiation with discussion of its probable causes and possible agricultural consequences. Agricultural and Forest Meteorology 107(4): 255 – 278

Torres O, Herman JR, Bhartia PK, and Sinyuk A (2002a) Aerosol properties from EP-TOMS near UV observations. Advances in Space Research 29: 1771 – 1780

Torres O, Herman JR, Bhartia PK, and Sinyuk A (2002b) A long term record of aerosol optical thickness from TOMS observations and comparison to AERONET measurement. Journal of Atmospheric Science 59: 398 – 413

Tzortziou M, Krotkov NA, Cede A, Herman JR, and Vasilkov A (2008) A new technique for retrieval of tropospheric and stratospheric ozone profiles using sky radiance measurements at multiple view angles: Application to a Brewer spectrometer. Journal of Geophysical Research 113:D06304, doi:10.1029/2007JD009093

Wenig MO, Bucsela EJ, Celarier EA, Gleason JF, Cede AM, Herman JR, Veefkind P, and Brinksma E (2006) Validation study of two years of OMI NO_2 data. Advanced Environmental Monitoring

WMO (World Meteorological Organization) (1999) Scientific assessment of ozone depletion: 1998. Global Ozone Research and Monitoring Project, Report No. 50, Geneva

WMO (2003) Scientific assessment of ozone depletion: 2002. Global Ozone Research and Monitoring Project, Report No. 47, Geneva

WMO (2007) Scientific assessment of ozone depletion: 2006. Global Ozone Research and Monitoring Project, Report No. 50, Geneva

Zerefos C, Balis D, Tzortziou M, Bais A, Tourpali K, Meleti1 C, Bernhard G, and Herman J (2001) A note on the interannual variations of UV-B erythemal doses and solar irradiance from ground-based and satellite observations. Annales Geophysicae 19: 115 – 120

Zuev VV, Bondarenko SL (2001) Relationship between long-period variability of atmospheric ozone layer with wood density variations caused by UV-B radiation. Atmospheric and Oceanic Optics 12: 1 – 4